




Article

Earth Abundant Oxidation Catalysts for Removal of Contaminants of Emerging Concern from Wastewater: Homogeneous Catalytic Screening of Monomeric Complexes

Leslie Garcia ¹, Makynna R. Koper ¹, Somrita Mondal ¹, Joshua T. Priddle ¹, William A. Truong ¹, Elisabeth M. A. Allbritton ¹, Ashtyn G. McAdoo ¹, Desiray J. Cannon-Smith ¹, Neil L. Funwie ¹, Tuyet Hoang ¹, Inseo Kim ¹, David J. Hubin ¹, Jeanette A. Krause ², Allen G. Oliver ³ , Timothy J. Prior ⁴  and Timothy J. Hubin ^{1,*} 

¹ Department of Chemistry and Physics, Southwestern Oklahoma State University, Weatherford, OK 73096, USA

² Department of Chemistry, University of Cincinnati, Cincinnati, OH 45220, USA

³ Department of Chemistry and Biochemistry, University of Notre Dame, Notre Dame, IN 46556, USA

⁴ Department of Chemistry, School of Natural Sciences, University of Hull, Kingston Upon Hull HU6 7RX, UK

* Correspondence: tim.hubin@swosu.edu

Abstract: Twenty novel Mn, Fe, and Cu complexes of ethylene cross-bridged tetraazamacrocycles with potentially copolymerizable allyl and benzyl pendant arms were synthesized and characterized. Multiple X-ray crystal structures demonstrate the cis-folded pseudo-octahedral geometry forced by the rigidifying ethylene cross-bridge and show that two cis coordination sites are available for interaction with substrate and oxidant. The Cu complexes were used to determine kinetic stability under harsh acidic and high-temperature conditions, which revealed that the cyclam-based ligands provide superior stabilization with half-lives of many minutes or even hours in 5 M HCl at 50–90 °C. Cyclic voltammetry studies of the Fe and Mn complexes reveal reversible redox processes indicating stabilization of Fe²⁺/Fe³⁺ and Mn²⁺/Mn³⁺/Mn⁴⁺ oxidation states, indicating the likelihood of catalytic oxidation for these complexes. Finally, dye-bleaching experiments with methylene blue, methyl orange, and rhodamine B demonstrate efficient catalytic decolorization and allow selection of the most successful monomeric catalysts for copolymerization to produce future heterogeneous water purification materials.

Keywords: dye bleaching; oxidation catalyst; cross-bridged tetraazamacrocycle



Citation: Garcia, L.; Koper, M.R.; Mondal, S.; Priddle, J.T.; Truong, W.A.; Allbritton, E.M.A.; McAdoo, A.G.; Cannon-Smith, D.J.; Funwie, N.L.; Hoang, T.; et al. Earth Abundant Oxidation Catalysts for Removal of Contaminants of Emerging Concern from Wastewater: Homogeneous Catalytic Screening of Monomeric Complexes. *Molecules* **2023**, *28*, 6466. <https://doi.org/10.3390/molecules28186466>

Academic Editors: Marco Pellegrini, Cesare Sacconi and Alessandro Guzzini

Received: 8 July 2023

Revised: 28 August 2023

Accepted: 4 September 2023

Published: 6 September 2023



Copyright: © 2023 by the authors. Licensee MDPI, Basel, Switzerland. This article is an open access article distributed under the terms and conditions of the Creative Commons Attribution (CC BY) license (<https://creativecommons.org/licenses/by/4.0/>).

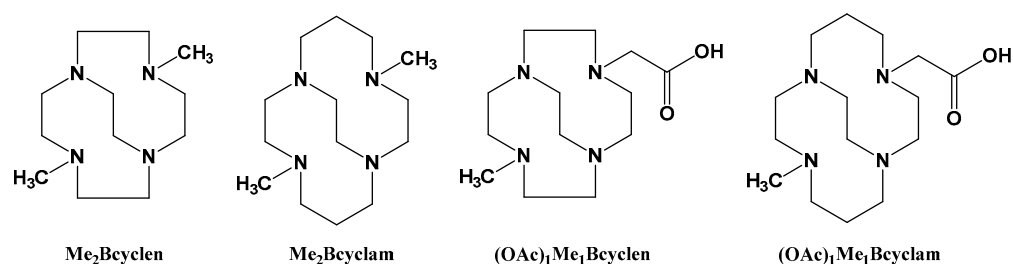
1. Introduction

Organic dyes have extensive applications in several industries such as food, pharmaceuticals, textiles, and cosmetics and thus are often the subject of academic scientific research focused on these same areas [1–4]. However, these dyes are potentially toxic in nature. Consequently, dyes in wastewater can cause severe damage to the aquatic environment as well as living organisms including humans. In order to overcome this environmental harm, dye degradation studies have been a topic of scientific interest over the past several decades [5–7]. Different methods have been implemented for dye degradation, e.g., oxidation of organic dyes using transition metal ions via the “Fenton” mechanism [8] and photocatalysis using semiconductor metal oxides and sulfides [9,10]. However, these conventional methods may suffer from several diverse drawbacks, depending on each specific system. Examples of issues hampering dye degradation systems include stability over a narrow pH range, low surface area, high cost, and limited applicability in visible light [8,11].

Transition metal complexes with cross-bridged macrocyclic ligands have been broadly explored for both research purposes and commercial purposes. Cross-bridged tetraazamacrocyclic transition metal complexes have been a prevalent candidate for substrate- and

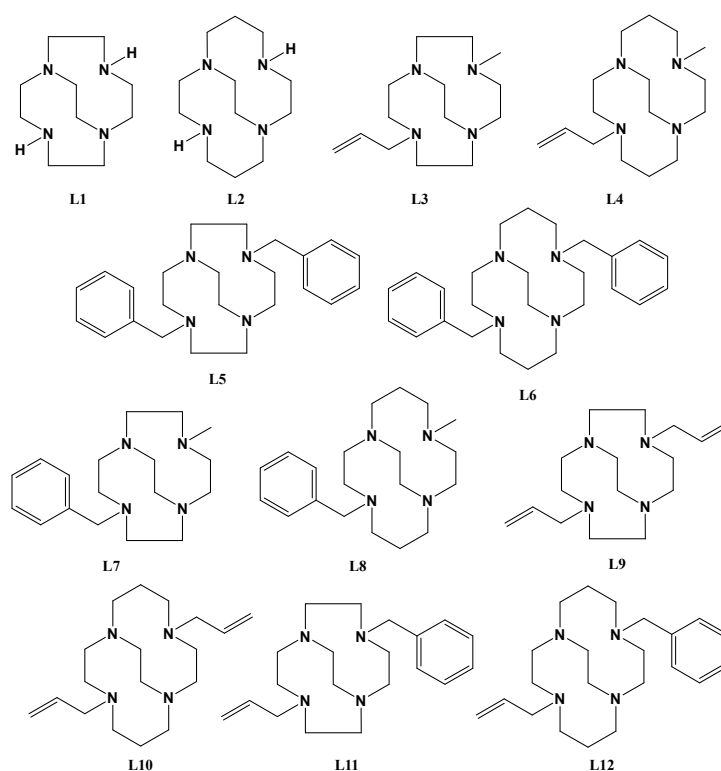
mechanism-flexible oxidation catalysis over the past two decades [12–22]. The ethylene cross-bridged tetraazamacrocycle transition metal complexes have been well-explored in biomedical imaging [23–31] and for anti-cancer therapy [32,33], owing to their extreme kinetic stability. However, studies pertaining to their dye-bleaching application have been limited.

The Busch catalyst, a Mn complex of the di-methylated ethylene cross-bridged cyclam **Me₂Bcyclam** (Scheme 1) [14], is a patented catalyst used for activation of peroxide or oxygen in water. In our previous study, we reported the functionalization of the original Busch catalyst with methyl and -OAc groups at the non-cross-bridged nitrogen atoms (Scheme 1) and their application in the degradation of three model dyes, namely, methyl orange, Rhodamine B, and methylene blue [34].



Scheme 1. Previously studied ethylene cross-bridged tetraazamacrocyclic ligands.

Building on our previous studies, our current study reports on the functionalization of the tetraazamacrocyclic ligand with different combinations of allyl, benzyl, and methyl groups at the non-cross-bridged nitrogen atoms (Scheme 2) and their respective Fe, Mn, and Cu complexes. The synthetic routes are facile and cost effective with significant synthetic yield. The ligands and their corresponding complexes were characterized using ¹H and ¹³C NMR (Figures S1–S12), LCMS, elemental analysis, X-ray crystallography, and cyclic voltammetry. Further, we have performed acid decomplexation studies on the copper complexes in order to determine their kinetic stability (Figure S13).



Scheme 2. L1–L12 structures used in this work.

In addition, we have expanded our efforts in exploring the ability of the metal complexes (typically Fe and Mn) to degrade the model dyes identified above. Most of the catalysts displayed significant activity in the degradation of all three dyes at 1 mM dye concentration. Thus, these metal complex catalysts can be practically applied for cheap and convenient bleaching of organic dyes, which can overcome the disadvantage of existing traditional photocatalysts.

Heterogeneous catalysis includes some liquid- or gas-phase reaction on a solid surface. Currently, heterogeneous catalysis is widely explored both in academic research and industry owing to its advantage of recyclability and easy separation of product [35]. In such cases, catalytic activity depends on many factors, such as particle size, surface area, stoichiometry, and topology of the designed catalysts. Different methods, e.g., non-covalent immobilization of catalysts within porous zeolites, clays, or embedding into silica or carbon; using a metal-organic framework (MOF) structure; and copolymerization through formation of covalent bonds, have been used to make catalysts heterogeneous [36–39]. The method of grafting or immobilization has drawbacks such as poor selectivity and catalytic activity. Therefore, direct heterogenization through covalent bond formation is a potential method to synthesize robust heterogeneous catalysts [36]. Rigidity of the building blocks associated with strong covalent bonds is highly desirable for stability of heterogeneous polymeric frameworks [40].

Attaching allyl and benzyl functional groups furthers the goal to explore the polymerization of our catalysts through covalent bond formation. These ligands were chosen as potential co-monomers that could be used to transform the homogeneous catalysts discussed in this paper into polymeric, heterogeneous catalysts. Thus, this study may lead to the successful design of a series of potential heterogeneous catalysts for degradation of organic pollutants leading to wastewater purification in a simple, convenient, and cost-effective way. The polymerization, characterization, and efficacy of these heterogeneous materials are the subject of ongoing work and will be disclosed in later publications. Below, we comment on each planned polymerization reaction type to explain why benzyl and allyl pendant arms have been utilized for this future work.

The Friedel–Crafts reaction is a historically important method of activating and substituting aromatic rings through the action of a metal catalyst [41]. When a di-functional alkyl halide, such as dichloromethane, is used, a Friedel–Crafts polymerization can be used to link monomeric aromatics, such as macrocyclic ligands that contain a benzyl group [42]. Specifically, the benzyl pendant arms may be polymerized by Friedel–Crafts polymerization following the work of Yoon, where salphen coordination complexes were polymerized through their aromatic rings [36]. Application of this method of polymerization to our benzyl ligands is ongoing in our lab.

Alkene functional groups are the prototypical polymerizable entity, with the ability to polymerize as catalyzed by heat, acid, base, and other prompts [43]. Allyl pendant arms have a terminal alkene functional group for this purpose within our experimental design. The allyl-pendant-armed ligands and complexes can copolymerize following the work of Zuo for ethylene glycol di-methacrylate (EGDMA) polymerization [44]. This copolymerization has been quite successful in our hands and will be the subject of future manuscripts.

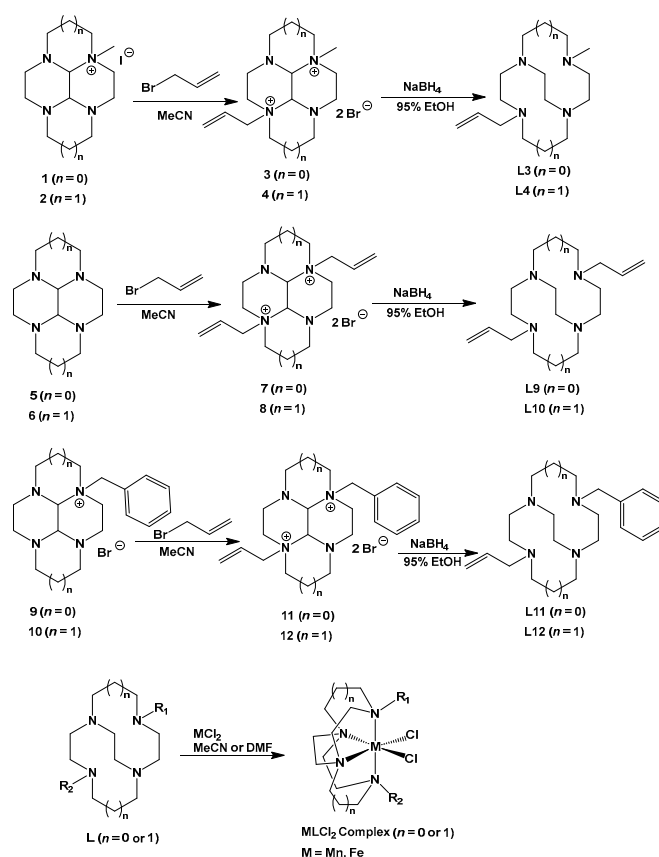
2. Results and Discussion

2.1. Synthesis

Ligands L1 [45], L2 [45], L5 [45], L6 [45], L7 [33], and L8 [32] were synthesized by literature procedures. Metal complexes MnL1Cl₂, FeL1Cl₂, MnL2Cl₂, FeL2Cl₂, MnL5Cl₂, FeL5Cl₂, MnL6Cl₂, FeL6Cl₂ [13], and FeL8Cl₂ [46] were prepared as previously published.

The homogeneous ligands and catalysts were produced according to Scheme 3, following synthetic methods that are now common for synthesizing cross-bridged tetraaza-macrocycles. Generally, the tetracyclic glyoxal-tetraazamacrocyclic condensate (Scheme 3, structures 5 or 6) can be mono- or di-alkylated by haloalkyl electrophiles. Mono-alkylation

is often controlled by low numbers of equivalents of the alkylating agent and non-polar solvent (THF), which causes the mono-quaternary salt to precipitate and avoid further reaction. The mono-methylated compounds **1** and **2** were prepared according to the literature [47,48], as were mono-benzylated compounds **9** and **10** [48]. Mono-alkylated compounds were then reacted with excess allyl bromide in more polar solvents (CH₃CN), at longer reaction times, and in some cases at higher temperatures, to produce di-quaternary mono-allylated products **3**, **4**, **11**, and **12**. Reductive ring cleavage with NaBH₄ produced the cross-bridged ligands **L3**, **L4**, **L11**, and **L12**. Di-allyl ligands **L9** and **L10** were made from **5** and **6** using excess allyl bromide to produce **7** and **8**, which were also reduced to the corresponding cross-bridged tetraazamacrocycle ligand.



Scheme 3. Combined synthetic scheme for the synthesis of new ligands and all metal complexes.

Complexation of all ligands was carried out using anhydrous CuCl₂, FeCl₂, or MnCl₂ in an inert atmosphere glovebox in CH₃CN or DMF. Cross-bridged tetraazamacrocycles are proton sponges, so anhydrous conditions and aprotic solvents are generally required to successfully make their Fe and Mn complexes [49]. Yields were often in the 50% range, as the products in most cases precipitated directly from the reaction. Identity and purities were established by electrospray mass spectroscopy and elemental analysis. Copper complexes were synthesized in order to probe the kinetic stability imparted by these ligands. This was accomplished by the published method using HCl at high concentrations (1 M or 5 M) and high temperatures up to 90 °C to decomplex the ligand. Comparisons to other known ethylene cross-bridged tetraazamacrocycle copper complexes can then place a new ligand in the hierarchy of kinetic stabilization ability.

2.2. X-ray Crystal Structures

Crystal data for all structures are found in Table 1, while selected bond lengths and angles are compiled in Table 2.

Table 1. Crystal data for X-ray crystal structures.

Identification code	[MnL1Cl ₂]	[MnL3Cl ₂]	[FeL3Cl ₂]	L8-precursor	[MnL9Cl ₂]	[MnL11Cl ₂]	[FeL11Cl ₂]. 2MeCN
Empirical formula	C ₁₀ H ₂₂ Cl ₂ MnN ₄	C ₁₄ H ₂₈ Cl ₂ MnN ₄	C ₁₄ H ₂₈ Cl ₂ FeN ₄	C ₂₀ H ₃₄ I ₂ N ₄ O ₂	C ₁₆ H ₃₀ Cl ₂ MnN ₄	C ₂₀ H ₃₂ Cl ₂ MnN ₄	C ₂₂ H ₃₅ Cl ₂ FeN ₅
Formula weight	324.15	378.24	379.15	616.31	404.28	454.33	496.30
Temperature/K	120	120	120	150	120	120	120
Crystal system	monoclinic	orthorhombic	orthorhombic	monoclinic	triclinic	monoclinic	orthorhombic
Space group	Cc	P2 ₁ 2 ₁ 2 ₁	P2 ₁ 2 ₁ 2 ₁	P2 ₁ /n	P-1	P2 ₁ /c	Pnma
a/Å	12.3081(13)	7.6390(4)	7.6198(5)	9.5389(10)	8.5540(11)	8.4238(4)	14.4316(7)
b/Å	10.1119(13)	12.0399(6)	11.9637(8)	16.9155(17)	13.2482(17)	13.5803(6)	8.9132(5)
c/Å	11.2029(12)	18.6843(10)	18.6306(14)	14.7768(14)	17.920(2)	18.6065(8)	19.5405(10)
α/°	90	90	90	90	107.492(2)	90	90
β/°	96.578(2)	90	90	91.479(4)	95.600(2)	98.507(2)	90
γ/°	90	90	90	90	97.994(2)	90	90
Volume/Å ³	1385.1(3)	1718.45(15)	1698.4(2)	2383.5(4)	1897.0(4)	2105.12(16)	2513.5(2)
Z	4	4	4	4	4	4	4
ρ _{calc} /gcm ⁻³	1.554	1.462	1.483	1.717	1.416	1.434	1.311
μ/mm ⁻¹	1.324	1.078	1.202	3.350	0.982	0.894	0.831
F(000)	676.0	796.0	800.0	1216.0	852.0	956.0	1048.0
Crystal size/mm ³	0.355 × 0.247 × 0.142	0.213 × 0.15 × 0.078	0.287 × 0.134 × 0.127	0.05 × 0.02 × 0.01	0.253 × 0.154 × 0.05	0.253 × 0.169 × 0.078	0.216 × 0.169 × 0.088
Radiation/Å	MoKα, 0.71073	MoKα, 0.71073	MoKα, 0.71073	Synchrotron, 0.7749	MoKα, 0.71073	MoKα, 0.71073	MoKα, 0.71073
2θ range for data collection/°	5.228 to 56.576	4.024 to 56.618	4.046 to 56.798	3.992 to 52.228	2.41 to 56.584	3.728 to 56.632	3.508 to 56.726
Index ranges	-16 ≤ h ≤ 14 -13 ≤ k ≤ 13 -14 ≤ l ≤ 14	-10 ≤ h ≤ 10 -16 ≤ k ≤ 16 -24 ≤ l ≤ 24	-10 ≤ h ≤ 9 -15 ≤ k ≤ 15 -24 ≤ l ≤ 24	-10 ≤ h ≤ 10 -19 ≤ k ≤ 19 -16 ≤ l ≤ 16	-11 ≤ h ≤ 11 -17 ≤ k ≤ 17 -23 ≤ l ≤ 23	-11 ≤ h ≤ 11 -18 ≤ k ≤ 18 -24 ≤ l ≤ 24	-19 ≤ h ≤ 19 -11 ≤ k ≤ 11 -26 ≤ l ≤ 26
Reflections collected	13204	31559	41891	37933	29491	49812	46814
Independent reflections	3268	4259	4239	3652	9415	5246	3344
R _{int}	0.0178	0.0520	0.0400	0.1904	0.0370	0.0340	0.0444
Data/restraints/parameters	3268/2/167	4259/0/192	4239/0/192	3652/0/269	9415/41/437	5246/0/244	3344/235/201
Goodness-of-fit on F ²	1.042	1.180	1.064	1.037	1.005	1.089	1.031
Final R indexes [I ≥ 2σ(I)]	R ₁ = 0.0131 wR ₂ = 0.0319	R ₁ = 0.0400 wR ₂ = 0.0740	R ₁ = 0.0385 wR ₂ = 0.0920	R ₁ = 0.0617 wR ₂ = 0.1579	R ₁ = 0.0307 wR ₂ = 0.0591	R ₁ = 0.0264 wR ₂ = 0.0603	R ₁ = 0.0284 wR ₂ = 0.0652
Final R indexes [all data]	R ₁ = 0.0133 wR ₂ = 0.0320	R ₁ = 0.0445 wR ₂ = 0.0751	R ₁ = 0.0401 wR ₂ = 0.0931	R ₁ = 0.0820 wR ₂ = 0.1757	R ₁ = 0.0499 wR ₂ = 0.0645	R ₁ = 0.0294 wR ₂ = 0.0615	R ₁ = 0.0372 wR ₂ = 0.0693
Largest diff. peak/hole/e Å ⁻³	0.18/−0.12	0.37/−0.52	0.93/−0.57	1.03/−0.74	0.33/−0.51	0.39/−0.22	0.30/−0.23
Flack parameter	0.077(10)	0.32(3) *(racemic twin)	0.47(3) *(racemic twin)	none	none	none	none

[MnL1Cl₂] crystallizes as well-formed colorless blocks in the non-centric space group Cc with a single molecule in the asymmetric unit. This space group was confirmed by the Flack parameter; the crystal structure determination was particularly good, with R = 1.33% and wR(F²) = 3.20% for all observed data.

The four nitrogen atoms of the ligand all coordinate to the central Mn²⁺ ion (Figure 1). The coordination is completed by two chloride ions to give a rather distorted octahedral geometry at the metal. There is some variation in the Mn-N bond lengths; N1-Mn1 and N3-Mn1 are 2.2761(14) and 2.2935(13) Å, respectively, while those nitrogen atoms joined by the bridge form longer bonds: N2-Mn1 = 2.3255(14) Å and N4-Mn1 = 2.3401(13) Å. The N-Mn-N bond angles for adjacent nitrogen atoms lie in the range of 72.80(5) to 77.18(5)°.

but the Mn ion lies somewhat outside the pocket of the ligand such that the angle of N1-Mn1-N3 is $142.60(5)^\circ$.

Table 2. Details of selected bond lengths and angles.

Structure	M-N1/Å M-N3/Å	M-N2/Å M-N4/Å	N1-M-N3/ $^\circ$ N2-M-N4/ $^\circ$
[Mn(L1)Cl ₂]	2.2761(14) 2.2935(13)	2.3255(14) 2.3041(13)	142.60(5) 73.49(5)
[Mn(L3)Cl ₂]	2.392(3) 2.313(3)	2.302(3) 2.314(3)	142.48(10) 74.85(10)
[Fe(L3)Cl ₂]	2.320(3) 2.257(3)	2.235(4) 2.233(4)	146.15(12) 77.20(11)
[Fe(L5)(OAc) ₂] Ref: [50]	2.3024(10) 2.3024(9)	2.2091(10) 2.2228(11)	148.84(4) 77.91(4)
[Mn(L9)Cl ₂]	Mn1: 2.3378(13) 2.3242(14)	Mn1: 2.2706(14) 2.2981(13)	Mn1: 144.69(5) 74.86(5)
	Mn2: 2.3510(14) 2.3786(15)	Mn2: 2.3138(14) 2.2873(14)	Mn2: 143.88(5) 74.15(5)
[Mn(L11)Cl ₂]	2.4019(11) 2.3935(11)	2.3090(11) 2.2834(11)	143.56(4) 74.09(4)
[Fe(L11)Cl ₂] · 2MeCN	2.2705(15) 2.262(2)	2.278(3) 2.169(3)	148.85(7) 77.38(12)

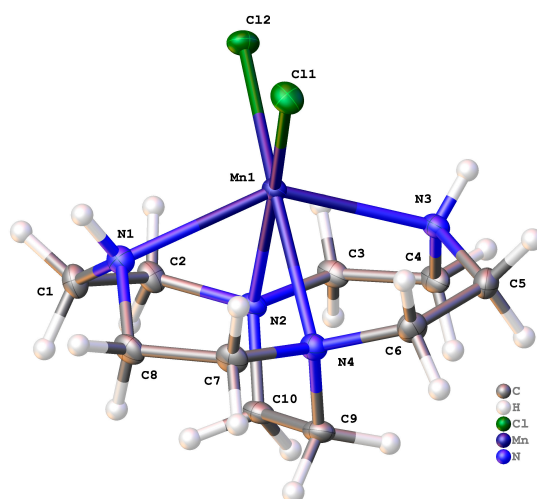


Figure 1. Asymmetric unit of [MnL1Cl₂] with atoms drawn as 50% probability ellipsoids.

In the solid state, there are hydrogen bonds (N1-H1...Cl2 and N3-H3...Cl1) between adjacent molecules, which form hydrogen-bonded tapes that run parallel to the crystallographic *c* axis.

[MnL3Cl₂] crystallizes in the chiral space group *P*2₁2₁2₁ with a single molecule in the asymmetric unit. This space group was identified from the systematic absences and the structure refined as a racemic twin with twin fractions 0.68 and 0.32(2). There was a very good fit to the observed data, with *R* = 4.45% and *wR*(*F*²) = 7.51% for all data.

The coordination about the Mn²⁺ ion is very similar to that in [MnL1Cl₂]; the central ion is coordinated by four nitrogen atoms from the ligand and two cis chlorides in a heavily distorted octahedral arrangement (Figure 2). However, there is a change in the relative lengths of the Mn-N bonds. In contrast to [MnL1Cl₂], here, Mn1-N1 is 2.392(3) Å and

Mn1-N3 is 2.313(3) Å, but Mn1-N2 and Mn1-N4 are 2.302(3) and 2.314(3) Å, respectively. It appears that addition of substituents to the non-bridged nitrogen atoms extends the Mn-N bond lengths, presumably on steric grounds. It is notable that the methylene group (C11) and the methyl group (C14) are aligned so that H···Cl distances are approximately 3.1 Å, which may signify an interaction. The bond lengths of C11-C12 and C12-C13 in the allyl group are 1.507(5) and 1.316(5) Å, respectively, confirming the allyl group has indeed been added intact. C-H···Cl interactions are formed from the two bound chlorides to a pair of hydrogen atoms attached to one side of the ethylene bridge of an adjacent molecule related by a translation of *a*. This interaction is repeated to generate tapes of molecules that run parallel to the crystallographic *a* axis. Between these tapes, there are further C-H···Cl interactions that assemble the molecules into a dense hydrogen-bonded array.

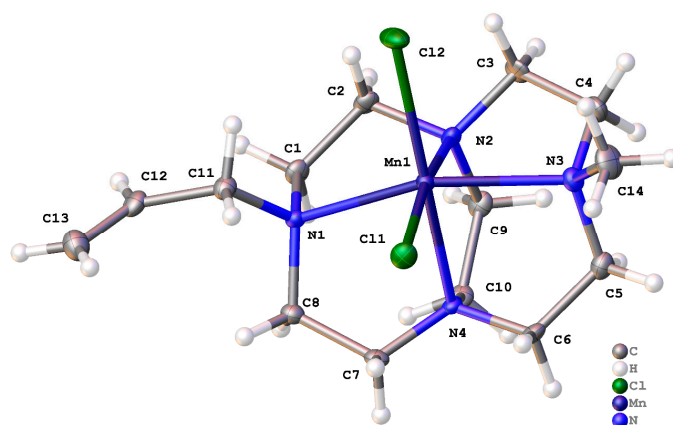


Figure 2. Asymmetric unit of $[\text{MnL3Cl}_2]$ with atoms drawn as 50% probability ellipsoids.

$[\text{FeL3Cl}_2]$ adopts the same structure as $[\text{MnL3Cl}_2]$ in space group $P2_12_12_1$. Each of the two structures is close to being centrosymmetric but is not. The systematic absences do not suggest any other space group, but some classes of data are systematically weak but not absent. It is possible to derive a centrosymmetric model in $Pnma$ in which the whole molecule is disordered over a mirror plane. The fit is much poorer and there are a large number of systematic absence violations that preclude a centrosymmetric model. The final fit in $P2_12_12_1$ is good, with $R = 4.01\%$ and $wR(F^2) = 9.30\%$ for all data. The coordination about the metal is very similar to the Mn analogue, with Fe1-N1 and Fe1-N3 distances being 2.320(3) and 2.257(3) Å, respectively. The bonds lengths from nitrogen atoms at the ethylene bridge are 2.235(4) and 2.233(4) Å. The Fe1-N1 and Fe1-N3 bonds subtend an angle of $146.15(12)^\circ$ at the iron center.

We have previously reported the structure of $[\text{FeL5}(\text{OAc})_2]$ [50]. The coordination about the metal is very similar, except that the two chlorides are replaced by a pair of strictly mono-dentate acetate ligands. The iron to nitrogen bond lengths are 2.2091(10) and 2.2228(11) Å for the nitrogens at the ethylene bridge. The Fe-N bond length for the nitrogen atoms that have the benzyl substituents (N1 and N3) are 2.3024(10) and 2.3024(9) Å (*sic*), respectively. The Fe is slightly better contained within the pocket of the macrocycle so that the N1-Fe-N3 bond angle is $148.84(4)^\circ$.

A crystal structure of the known mono-methylated, mono-benzylated cyclam-glyoxal di-iodide [32] was obtained during the course of this work and is shown in Figure 3. The X-ray scattering was rather weak even though the data were collected using synchrotron radiation. However, the structure solves well in the centrosymmetric space group $P2_1/n$ with a single molecule in the asymmetric unit. The positive charge of the two tetraalkylammonium centers is balanced by two iodide ions. There is good evidence for disorder in the iodide positions and the single water molecule. In the solid state, the substituted cyclam ions are arranged in layers parallel to the $(1\ 0\ -1)$ plane and oriented so that they generate channels parallel to the crystallographic *a* direction. The water and iodide are found in these channels, between layers of ions.

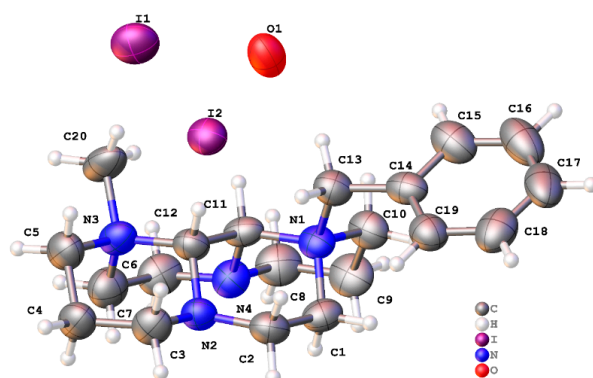


Figure 3. Asymmetric unit of L8 precursor with minor disorder not shown. Atoms are represented as 50% probability ellipsoids.

[MnL9Cl₂] crystallizes in the centrosymmetric space group *P*-1 with two unique molecules in the asymmetric unit ($Z' = 2$). Refinement of the model was straightforward, and minor disorder in one of the pendant allyl groups was dealt with using normal methods. The final fit was very good: $R = 4.99\%$ and $wR(F^2) = 6.45\%$ for all data. Similar to the earlier examples, the metal ion is found in a distorted octahedral coordination geometry with a pair of cis chloride ions, as shown in Figure 4.

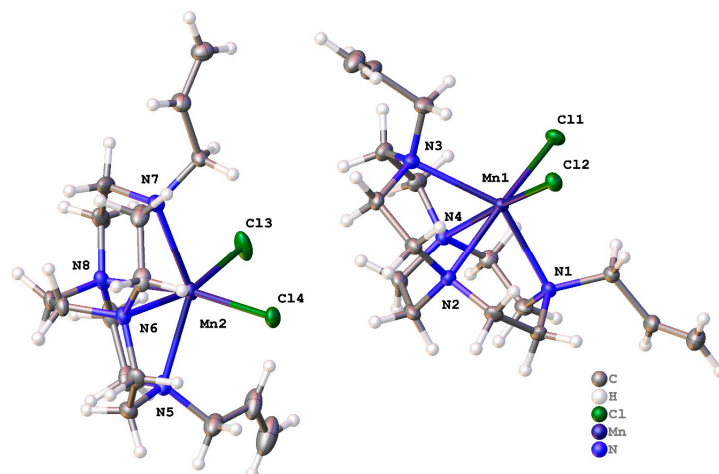


Figure 4. Asymmetric unit of [MnL9Cl₂] with minor disorder not shown. Atoms are represented as 50% probability ellipsoids.

There are small differences in the orientation of the ligands around the metal ions in the two unique complexes, but the differences are not substantial. The familiar distorted octahedral coordination is observed, and, as in other cases, the nitrogen atoms joined by the ethylene bridge form shorter bonds to the metal than those bearing allyl substituents, as shown in Table 2, although the bonds about Mn2 are longer than those about Mn1.

The two unique complexes in the asymmetric unit form a hydrogen-bonded dimer through C-H...Cl interactions between bound chlorides of one complex and hydrogens from the ethylene bridge of the other. One of these hydrogen bonds is bifurcated such that the chloride is a hydrogen bond acceptor from two C-H groups. There is a further single trifurcated C-H...Cl hydrogen bond between pairs of these dimers, which assembles them into chains that run parallel to the (110) direction. Between these chains, additional C-H...Cl interactions generate a hydrogen-bonded three-dimensional network.

The crystal structure of [MnL11Cl₂] is centrosymmetric (space group *P*2₁/*c*) but in other respects is similar to the other complexes described above. Once again, the fit of the model to observed data is excellent: $R = 2.94\%$ and $wR(F^2) = 6.16\%$ for all data. The

asymmetric unit contains a single Mn^{2+} ion with four nitrogen atoms from the ligand bent away from two cis chloride ions, as shown in Figure 5. Here, the nitrogen atoms of the ethylene bridge (N2 and N4) are substantially closer to the metal than N1 and N3. Mn-N2 and Mn-N4 bonds are approximately 2.30 Å, but those for N1 and N3 are elongated with values at approximately 2.40 Å (Table 2).

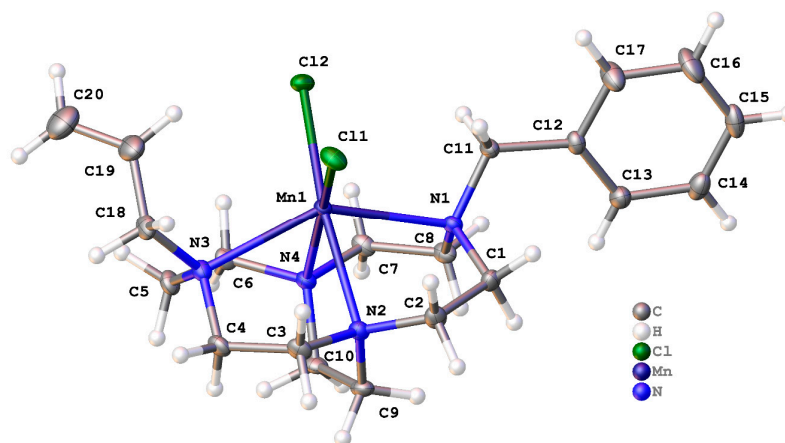


Figure 5. Asymmetric unit of $[\text{MnL11Cl}_2]$ with atoms represented as 50% probability ellipsoids.

In the solid state, extensive hydrogen bonding between bound chloride and C-H groups produces hydrogen-bonded sheets in the xy plane. There are van der Waals interactions between layers, and close approach of C-H to the benzyl substituent may give rise to further weak C-H $\cdots\pi$ interactions.

$[\text{FeL11Cl}_2]$ crystallizes with acetonitrile within the structure to give the formula of $[\text{FeL11Cl}_2] \cdot 2\text{MeCN}$. The space group is $Pnma$ (centrosymmetric), and the asymmetric unit contains one half complex that is disordered over a mirror plane. This added significant complication to the modeling of the observed electron density, but a satisfactory fit was possible using standard methods of disorder modeling: $R(F) = 3.72\%$ and $wR(F^2) = 6.93\%$ (all data). The asymmetric unit is shown in Figure 6, and a representation of the whole complex appears in Figure 7. The basic coordination about the Fe^{2+} ion is similar to that in the equivalent Mn^{2+} example, but the M-N bonds are shorter, although the trend of nitrogen atoms on the ethylene bridge having shorter bond lengths is preserved, as shown in Table 2.

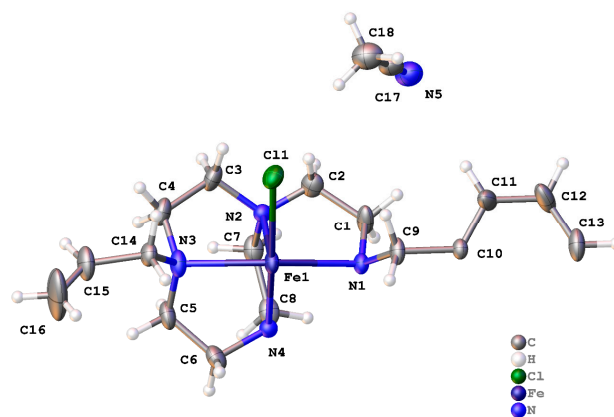


Figure 6. Asymmetric unit of $[\text{FeL11Cl}_2] \cdot 2\text{MeCN}$ with atoms represented as 50% probability ellipsoids.

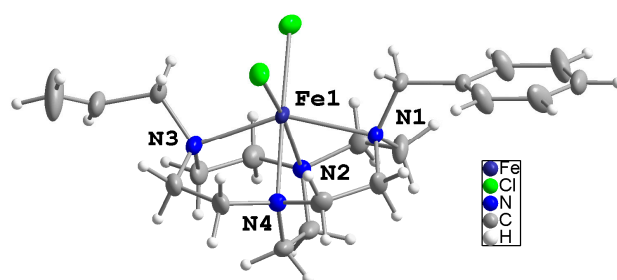


Figure 7. Complete [FeL11Cl₂] complex with atoms represented as 50% probability ellipsoids.

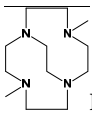
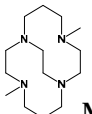
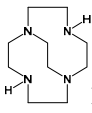
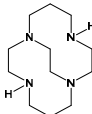
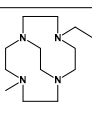
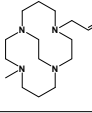
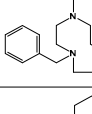
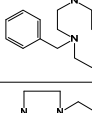
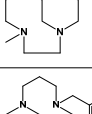
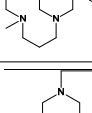
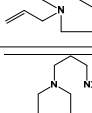
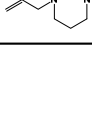
Focusing on the metrics about the metal centers of the **L1** and **L11** ligands (Table 2), it is apparent that the addition of substituents to the ethylene-bridged cyclen changes the coordination behavior of the ligand. [MnL1Cl₂] contains the unsubstituted ethylene-bridged cyclen, and the nitrogen atoms (N2 and N4) of the bridge are further from the metal than the two NH donors (N1 and N3). The bite angle of the two bridge nitrogen atoms is the smallest of these complexes described here. Adding substituents to N1 and N3 reverses the trend in bond lengths; in all of the other complexes, the mean bond lengths for M-N1 and M-N3 are longer than those for M-N2 and M-N4.

A trend in the bond lengths and angles is observed for the Mn²⁺ and Fe²⁺ complexes of ligands **L3** and **L11**. For **L3**, the Fe-N bond lengths are ~2.5% shorter than for Mn-N. Examination of equivalent M²⁺ structures in the CCDC [51] reproduces this trend, namely M-N bonds of the bridge are ~3.3% longer for Fe²⁺, while for the other nitrogen atoms the bond lengths are 2.0% longer. Further, the ethylene bridge bite angle (N2-M-N4) is significantly smaller for Mn, while the N1-M-N3 angle is larger for Fe. The data in the CCDC confirm this as well; the N2-M-N4 and N1-M-N3 bite angles are 3.8% and 2.9% smaller for Mn²⁺, respectively. These changes signify that the Fe²⁺ resides deeper into the cavity of the macrocycle than Mn, presumably as a consequence of the smaller size of Fe²⁺. Similar trends are observed for **L11**; Fe-N bond lengths are substantially shorter than those of Mn-N. The bite angle of N2-M-N4 is larger for Fe (77.38(12)° vs. 74.09(4)° for Mn) and the N1-Fe-N3 angle is 148.85(7)° for Fe (143.56(4)° for Mn).

2.3. Acid Decomplexation Studies

CuLCl₂ or [CuLCl][PF₆] complexes of the novel ligands studied here were synthesized whenever possible (pure **L11** and **L12** complexes could not be synthesized and were excluded from this study). Decomplexation of such copper(II) complexes of cross-bridged tetraazamacrocycles under harsh conditions of strong acid and high temperature have become a standard method for examining the kinetic stability imparted by the ligand on metal complexes with these ligands [21–23,31,49,52–54]. Due to the proton sponge nature of these highly basic tetraamines, potentiometric titrations of metal complexation reactions in aqueous solution are generally not possible, as it is impossible to fully deprotonate the ligands in water. It is therefore necessary to conduct the kinetic evaluation under harsh acidic conditions (Table 3). Cu²⁺ is generally used, as the complexes are highly colored with only one d-d absorption band, which can easily be monitored using electronic spectroscopy, allowing the pseudo-first-order kinetic analysis and half-life calculations (see Experimental Section for details). Manganese(II) and iron(II) complexes themselves lack strong d-d absorption bands, making it impossible to perform the same experiments on them. Therefore, the copper(II) complex, with the constant being the Cu²⁺ ion itself, has been adopted as the standard used in order to compare the effect of each different cross-bridged ligand on stability. This is an imperfect system, but it gives relative ligand effects. It is not meant to imply that the Mn or Fe complexes would be as stable but to give the relative effects of the differing ligand structures on kinetic stability.

Table 3. Kinetic stability of [CuLCl₂] and [CuLCl]PF₆ complexes of ligands L1–L10 under harsh acidic conditions.

Ligand	Pseudo-First-Order Half-Life for Decomplexation of 1.000 mM Copper Complexes					References
	30 °C 1 M HCl	30 °C 5 M HCl	50 °C 5 M HCl	70 °C 5 M HCl	90 °C 5 M HCl	
 Me₂Bcyclen	36 min		<1 min			[55]
 Me₂EBC			7.3 day		79 min	[22,55]
 H₂Bcyclen (L1)	<1 min					[21]
 H₂Bcyclam (L2)	18.5 d		5.40 h [This work]		11.8 min	[54]
 Me₁Allyl₁Bcyclen (L3)	25 min					This work
 Me₁Allyl₁Bcyclam (L4)			2.33 h			This work
 Bn₂Bcyclen (L5)	4.2 h	7.8 min				[33,56]
 Bn₂Bcyclam (L6)			2.38 h	23.4 min		[33,56]
 Me₁Bn₁Bcyclen (L7)	24.8 min					This work
 Me₁Bn₁Bcyclam (L8)			15.05 h	1.4 h		This work
 Allyl₂Bcyclen (L9)	51.7 min					This work
 Allyl₂Bcyclam (L10)			1.86 h	15 min		This work

Cross-bridged cyclen copper complexes are not particularly stabilized by the topological complexity and rigidity imparted by the ethylene cross-bridge [56]. The small cavity does not allow for optimal complementarity between the small ligand and the Cu²⁺ cation [57]. Even though the cross-bridge does rigidify the ligand/complex, without good

complementarity, the rigidity effects do not result in large kinetic stability gains. The small cyclen macrocycle is rather rigid itself, with only ethylene chains and all five-membered chelate rings in the complex. Adding the cross-bridge simply distorts the pseudo-octahedral or square pyramidal structure, leading to minimal stabilization, if any at all, over the unbridged complexes [56]. Even so, it is interesting to probe the pendant arm effects on the stability of the copper complexes. Data were obtained, or were already available, for all cyclen complexes at 30 °C in 1 M HCl, allowing for direct comparison.

The simplest ethylene cross-bridged cyclen $H_2Bcyclen$ (**L1**) has a very short half-life of less than one minute, even in 1 M HCl acid conditions and at 30 °C [21]. The stability of the Cu^{2+} complexes increases in the following ligand order upon addition of substituents, making all tertiary nitrogen donors (Table 3) $H_2Bcyclen$ (**L1**) < $Bn_1Me_1Bcyclen$ (**L7**)~ $Allyl_1Me_1Bcyclen$ (**L3**) < **Me₂Bcyclen** < $Allyl_2Bcyclen$ (**L9**) < $Bn_2Bcyclen$ (**L5**). The trend(s) here are not completely transparent, but some comments can be made. It appears that a single Me group combined with one larger substituent is not optimal for stability, as **L7** and **L3** are only modestly stabilized. Two Me substituents (**Me₂Bcyclen**) give more stability, although the effect is not large. Finally, two larger allyl or Bn substituents on the ligand (**L9** and **L5**, respectively) impart even greater stability, with **L5** exhibiting the highest stability (4.2 h vs. 51.7 min).

Ethylene cross-bridged cyclam complexes are stabilized to a much greater extent by the topological complexity and rigidity of the ethylene cross-bridge. The complementarity match, (mostly a size effect) of the larger cyclam cavity for the Cu^{2+} ion allows stabilization through the additional constraint factors [56]. As such, the Cu-Bcyclam complexes are usually studied at higher acid concentration (5 M HCl) and at elevated temperature (50 °C, 70 °C, and 90 °C). For example, $Cu(Me_2Bcyclam)Cl^+$ has a half-life of 79 min even at 90 °C in 5 M HCl, conditions that quickly destroy the vast majority of transition metal complexes. Data were obtained, or were already available, for all cyclam complexes at 50 °C in 5 M HCl, allowing for direct comparison.

The stability of the Cu^{2+} cyclam complexes increases in the following ligand order (Table 3): $Allyl_2Bcyclam$ (**L10**) < $Allyl_1Me_1Bcyclam$ (**L4**)~ $Bn_2Bcyclam$ (**L6**) < $H_2Bcyclam$ (**L2**) < $Bn_1Me_1Bcyclam$ (**L8**) < **Me₂Bcyclam**. Interestingly, the bulkier substituents (Bn, allyl) actually appear to destabilize the copper complexes with the cyclam ring size, rather than stabilizing them as seen for the cyclen ligands. In fact, two of the three most stable complexes, with **L2** and **Me₂EBC**, have either only hydrogen or methyl substituents. Of the most stable cyclam complexes, **L8**, $Bn_1Me_1Bcyclam$ contains a single large Bn group. Though only a hypothesis, the poor size match of the cyclen systems may gain stability as large allyl and Bn groups block access by H^+ to the otherwise exposed (due to the severely distorted octahedral geometry) Cu^{2+} -N bonds that must protonate in order for metal decomplexation to occur. On the other hand, the much better complementarity of the cyclam systems leads to less distortion of the octahedral geometries. Here, the smaller substituents (H, Me) distort the Cu^{2+} -N bonds to a lesser extent, while the larger allyl and Bn substituents may disrupt the complementarity to a greater extent, leading to faster decomplexation. Regardless, what is observed is that the ethylene cross-bridged cyclam complexes, in particular, are remarkably kinetically stable under harsh acidic conditions, which would suggest oxidation catalysts (in the case of Fe and Mn) that should survive to function for significant lengths of time during the proposed water purification processes.

2.4. Cyclic Voltammetry

Cyclic voltammetry studies on 1.000 mM solutions of the Fe and Mn complexes in MeCN were carried out in order to correlate available reversible redox processes with their reactivity (Figures S14–S21). The results of these studies are presented in Table 4. Previous work on the Fe and Mn complexes of cross-bridged tetraazamacrocycles is included and has generally shown that higher oxidation catalyst reactivity is related to higher oxidation potentials for reaching the higher oxidation states of these metals. Copper complexes were not included in this cyclic voltammetry study, as they are not active oxidation catalysts.

Table 4. Redox potentials (V) vs. SHE (0.00 V) and ΔV (mV) for 1.000 mM solutions of the Fe and Mn complexes of L1–L12 in MeCN.

Complex	$E_{1/2}$ $M^{2+/3+}$ [V] (ΔV [mV])	$E_{1/2}$ $M^{3+/4+}$ [V] (ΔV [mV])	Reference
Fe(Me ₂ Bcyclen)Cl ₂	+0.036 (64)	----	[12]
Mn(Me ₂ Bcyclen)Cl ₂	+0.466 (70)	+1.232 (102)	[12]
Fe(Me ₂ Bcyclam)Cl ₂	+0.110 (63)	----	[12]
Mn(Me ₂ Bcyclam)Cl ₂	+0.585 (61)	1.343 (65)	[12]
[FeL1Cl ₂]	-0.055 (89)	----	[13]
[MnL1Cl ₂]	+0.389 (280)	not accessible in DMF	[13]
[FeL2Cl ₂]	-0.113 (78)	----	[13]
[MnL2Cl ₂]	+0.239 (79)	not accessible in DMF	[13]
[FeL3Cl ₂]	+0.094 (82)	----	This work
[MnL3Cl ₂]	+0.545 (71)	+1.338 (86)	This work
[FeL4Cl ₂]	+0.165 (96)	----	This work
[MnL4Cl ₂]	+0.628 (59)	+1.374 (83)	This work
[FeL5Cl ₂]	+0.071 (85)	----	[13]
[MnL5Cl ₂]	+0.400 (65)	not accessible in DMF	[13]
[FeL6Cl ₂]	+0.157 (85)	----	[13]
[MnL6Cl ₂]	+0.577 (72)	not accessible in DMF	[13]
[FeL7Cl ₂]	+0.065 (64)	----	This work
[MnL7Cl ₂]	+0.550 (76)	+1.355 (82)	This work
[FeL8Cl ₂]	+0.176 (86)	----	This work
[MnL8Cl ₂]	+0.609 (93)	+1.404 (92)	This work
[FeL9Cl ₂]	+0.114 (92)	----	This work
[MnL9Cl ₂]	+0.572 (68)	+1.385 (79)	This work
[FeL10Cl ₂]	+0.194 (59)	----	This work
[MnL10Cl ₂]	+0.616 (72)	+1.422 (83)	This work
[FeL11Cl ₂]	+0.130 (78)	----	This work
[MnL11Cl ₂]	+0.558 (72)	+1.390 (73)	This work
[FeL12Cl ₂]	+0.196 (72)	----	This work
[MnL12Cl ₂]	+0.619 (85)	+1.433 (92)	This work

The cyclic voltammetry data are useful in evaluating the oxidizing ability of the higher-valent oxidation states of these catalysts with the reversibility generally desirable for catalytic species. These ligands support Fe^{2+/3+} ions and Mn^{2+/3+/4+} ions with good reversibility in acetonitrile (see ESI for CV curves). A few complexes, those of L1, L2, L5, and L6, were only soluble in DMF, thus their data may have slight solvent effects and lack the Mn^{3+/4+} couple due to the limits of DMF solvent becoming oxidized itself. One trend that is quite consistent is that the smaller cyclen complex in a cyclen/cyclam pair having the same pendant arms is always easier to oxidize. This is likely a simple cavity size effect, with the smaller cyclen ring selecting for the smaller M³⁺ or M⁴⁺ cation and the larger cyclam ring selecting for the larger, lower-valent metal ion. Only the unsubstituted L1 and L2 show an inversion of this ring-size selectivity, which may be the result of less rigidity of these ligands due to having two secondary nitrogen donors, while all other ligands have all four nitrogen donors as more constrained tertiary nitrogen atoms.

Substituent effects are observed, although they are relatively small. For the best comparison, only those complexes examined in the same solvent (MeCN) are compared directly. For Fe complexes, replacing one methyl group with one benzyl group results in an increase in $\Delta E_{1/2}$ of ~ 0.03 – 0.06 V. For example, Fe(**Me₂Bcyclam**)Cl₂ and Fe**L8**Cl₂ have $E_{1/2}$ values of +0.110 V and +0.176 V, respectively. The change is a bit larger for Mn complexes, where $\Delta E_{1/2}$ of ~ 0.07 – 0.12 V is seen. For example, Mn(**Me₂Bcyclen**)Cl₂ and Me**L7**Cl₂ have $E_{1/2}$ Mn^{3+/4+} values of +1.232 V and +1.355 V, respectively. Replacing successive methyl groups with allyl groups for Fe complexes results in an increase in $\Delta E_{1/2}$ of ~ 0.04 – 0.06 V per allyl group. Fe(**Me₂Bcyclam**)Cl₂, Fe**L4**Cl₂, and Fe**L10**Cl₂ have $E_{1/2}$ values of +0.110 V, +0.165 V, and +0.194 V, respectively. The change is again larger for Mn complexes, where $\Delta E_{1/2}$ of ~ 0.06 – 0.12 V is seen. For example, Mn(**Me₂Bcyclen**)Cl₂, Mn**L3**Cl₂, and Mn**L9**Cl₂ have $E_{1/2}$ Mn^{3+/4+} values of +1.232 V, +1.338 V, and 1.385 V, respectively. These last two series show that the substituent effects are cumulative.

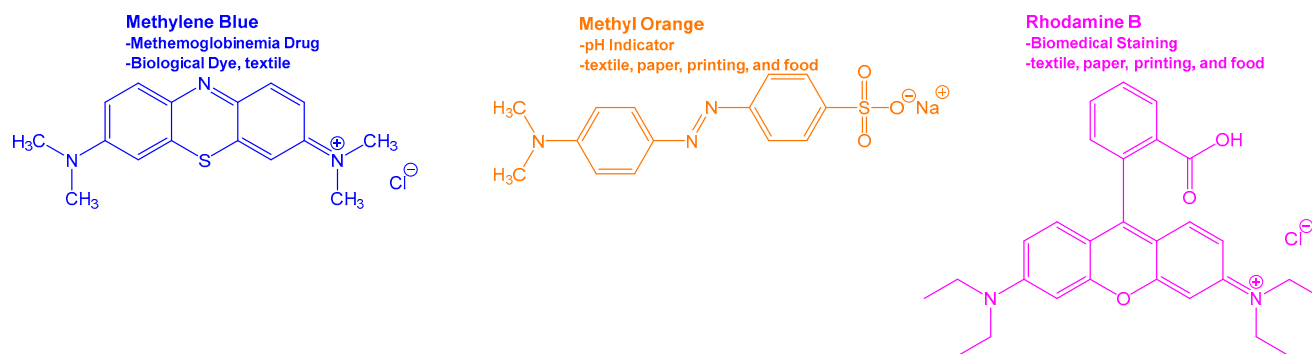
Interestingly, the highest oxidation potentials are found in the mixed pendant arm ligands **L11** and **L12**. The maximum $E_{1/2}$ value for an Fe^{2+/3+} couple in a cyclen-based complex was found for Fe**L11**Cl₂, with +0.130 V. The maximum $E_{1/2}$ value for an Fe^{2+/3+} couple in a cyclam-based complex was found for Fe**L12**Cl₂, with +0.196 V. The maximum $E_{1/2}$ value for an Mn^{3+/4+} couple in a cyclen-based complex was found for Mn**L11**Cl₂, with +1.390 V. This value is actually higher than the oxidation potential for the well-known Mn(**EBC**)Cl₂ catalyst (+1.343 V), showing that substituent choices can serve to replace ring-size effects in order to modify oxidation potential. The maximum $E_{1/2}$ value for an Mn^{3+/4+} couple in a cyclam-based complex was found for Mn**L12**Cl₂, with +1.433 V, a full 0.090 V higher than for the Mn(**Me₂Bcyclam**)Cl₂ catalyst (+1.343 V). Di-allyl ligands **L9** and **L10** similarly raise the respective oxidation potentials of their Fe and Mn complexes, though slightly less effectively than the Allyl₁Bn₁ ligands **L11** and **L12** (see Table 4). The main goal of adding these particular pendant arms was to investigate copolymerization reactions that could incorporate these catalysts into water-insoluble polymers for eventual use as heterogeneous water purification materials. However, increasing their oxidation potentials might be predicted to lead to more reactivity as oxidation catalysts, which is examined below.

Future electrochemical work will need to build off what has been learned: 1. the larger cyclam ligands support higher oxidation states in general, leading to (see below) higher oxidation catalysis reactivity and 2. pendant arm effects are minimal but maximized when both an allyl and benzyl pendant arm are present in the same complex. As we continue towards the goal of heterogeneous catalysts, we will need to discern if oxidation potentials are changed when the complexes are fixed into copolymeric materials, as has been observed previously [58,59]. Fortunately, many polymers are soluble in solvents such as DMF and THF in which cyclic voltammetry can be carried out [60]. We will endeavor to track the changes in cyclic voltammetry and how they track with oxidation efficiency for polymeric compounds in future work.

2.5. Dye-Bleaching Studies

The goal of our overall project is to develop catalysts capable of efficient removal of organic pollutants (contaminants of emerging concern, CEC) from wastewater via oxidation catalysis. Eventually, we hope to develop catalysts such as those disclosed here into heterogeneous catalytic materials via copolymerization using the allyl and benzyl pendant arms as sites of copolymerization to incorporate the Fe and Mn cross-bridge macrocycle complex cores into water-insoluble polymers for easy separation, or perhaps as cartridge-filling material for contaminated water to be passed through with purified water exiting the cartridge. In this work, we focus on screening a large number (24) of new complexes to determine their homogeneous oxidation catalytic ability prior to selecting lead compounds for copolymerization. We have selected three extensively used dyes [1,7,9,10] (Scheme 4), methylene blue (MB), methyl orange (MO), and Rhodamine B (RhB), as model organic pollutants for our degradation study using our metal–ligand

oxidation catalysts (metal = Fe and Mn with **L1–L12**) (Figures S22–S33). The two cationic dyes (MB and RhB) and the anionic dye (MO) have diverse functional groups including NMe_2^+ , $-\text{SO}_3^-$, $-\text{COOH}$, and $=\text{N}^+\text{Et}_2$. These oxidation catalysts were able to degrade all three of the dyes in the presence of hydrogen peroxide (H_2O_2) as the terminal oxidant. In a survey of many potential catalysts to identify lead compounds, it is not feasible to perform the dye-bleaching experiments for all complexes at a wide range of pHs due to time and resource constraints. We chose neutral pH 7 to conduct this screening study, as we knew the complexes and dyes were stable at this pH and that most natural and municipal water sources have pHs in the pH 6–8 range [61].



Scheme 4. Dyes used in the dye-bleaching studies.

Table 5 illustrates the average TOF values of control substances and oxidation catalysts for the degradation of methylene blue (MB), methyl orange (MO), and Rhodamine B (RhB). The eight complexes in red stand out among the rest as having at least one significantly higher-than-average TOF. Ranked order (1 being best) among these top eight catalysts are given in parentheses following each TOF value. The fifth column provides an overall ranked order based on an average rank order for the three dyes. For discussion purposes, the highest redox potential observed, and the kinetic stability half-life of the copper analogue (when available), are included in the table. Dye-bleaching plots, showing A_t/A_0 vs. time for all catalysts, can be found in the ESI, along with narrative observations for each ligand's Fe/Mn pair of complexes. Here, we will present a broader discussion of general trends and observations about what factors lead to better dye bleaching.

Observation 1: Manganese catalysts generally outperform iron catalysts, which is the case for ligands **L3–L4**, **L6–L10**, and **L12**. Ligands **L5** and **L11** gave similar activity for both metals. Only iron catalysts with **L1** and **L2** gave clearly superior results. It should be noted that **L1** and **L2** have two secondary nitrogen donors, which sterically allows for dimerization to occur [13], forming LFe-O-FeL and $\text{LMn-(O)}_2\text{-Mn}$ structures. Dimerization is sterically prevented by all alkyl substitutions of these hydrogen atoms, even methyl groups. It is likely that the Fe-O-Fe dimers are forming in the presence of H_2O_2 , as has been observed [13], and that these dimers are the active catalysts, as they have one open coordination site per Fe to interact with the oxidant and substrate. Perhaps the coordinatively saturated Mn dimers, lacking an open coordination site, are unable to act as catalysts. All other ligands, having alkyl groups in place of these hydrogens, are prevented from dimerizing [13], which allows the monomeric complexes to persist in solution and act as the oxidation catalysts, where Mn is more efficient than Fe, as has been proposed for the well-known $\text{MnMe}_2\text{BcyclamCl}_2$ catalyst [12].

Table 5. Turnover frequency (TOF) values, and other relevant parameters, for control and all 24 metal-complex catalysts for degradation of MB, MO, and RhB.

Catalyst	Average TOF for MB (h ⁻¹) (Rank among Top 8)	Average TOF for MO (h ⁻¹) (Rank among Top 8)	Average TOF for RhB (h ⁻¹) (Rank among Top 8)	Catalyst Rank Based on Average Rank Order for Top 8 Catalysts for All Three Dye TOFs	Highest Redox Potential Observed (Fe ³⁺ , Mn ³⁺ , or Mn ⁴⁺)	Half-Life of Cu ²⁺ Complex Under Acid Conditions (Cyclen Complexes in 1 M HCl, 30 °C; Cyclam Complexes in 5 M HCl, 50 °C)
H ₂ O ₂ only	0.018	0.034	0.002			
FeCl ₂ only	0.111	0.926	0.055			
MnCl ₂ only	0.003	0.518	0.047			
[FeL1Cl ₂]	0.54	1.33	0.31		−0.055 V	<1 min
[MnL1Cl ₂]	0.32	1.08	0.14		+0.389 V	<1 min
[FeL2Cl ₂]	1.21 (7)	31.35 (3)	3.62 (1)	3 (tie) (Avg = 3.67)	−0.113 V	5.40 h
[MnL2Cl ₂]	0.27	0.147	0.18		+0.239 V	5.40 h
[FeL3Cl ₂]	0.33	1.46	0.64		+0.94 V	25 min
[MnL3Cl ₂]	1.67 (5)	6.42 (8)	1.104 (7)	6 (Avg = 6.67)	+1.338 V	25 min
[FeL4Cl ₂]	0.35	1.26	0.63		+0.165 V	2.33 h
[MnL4Cl ₂]	2.03 (4)	16.26 (4)	1.05 (8)	4 (Avg = 5.33)	+1.374 V	2.33 h
[FeL5Cl ₂]	0.13	4.08	0.21		+0.071 V	4.2 h
[MnL5Cl ₂]	0.16	0.60	0.11		+0.400 V	4.2 h
[FeL6Cl ₂]	0.45	3.41	0.62		+0.157 V	2.38 h
[MnL6Cl ₂]	0.74 (8)	16.14 (5)	1.27 (5)	5 (tie) (Avg = 6)	+0.577 V	2.38 h
[FeL7Cl ₂]	0.13	0.083	0.13		+0.065 V	24.8 min
[MnL7Cl ₂]	2.64 (3)	8.32 (7)	2.34 (2)	3 (tie) (Avg = 3.67)	+1.355 V	24.8 min
[FeL8Cl ₂]	0.57	2.82	1.54		+0.176 V	15.05 h
[MnL8Cl ₂]	2.09 (3)	108.9 (1)	1.46 (4)	2 (Avg = 2.67)	+1.404 V	15.05 h
[FeL9Cl ₂]	0.35	0.77	0.92		+0.114 V	51.7 min
[MnL9Cl ₂]	0.53	3.13	0.35		+1.385 V	51.7 min
[FeL10Cl ₂]	0.171	2.2	0.35		+0.194 V	1.86 h
[MnL10Cl ₂]	1.23 (6)	9.40 (6)	1.16 (6)	5 (tie) (Avg = 6)	+1.422 V	1.86 h
[FeL11Cl ₂]	0.19	0.43	0.26		+0.130 V	n/a
[MnL11Cl ₂]	0.18	0.86	0.15		+1.390 V	n/a
[FeL12Cl ₂]	0.25	1.26	0.70		+0.196 V	n/a
[MnL12Cl ₂]	5.87 (1)	36.49 (2)	1.61 (3)	1 (Avg = 2.0)	+1.433 V	n/a

Observation 2: Cyclam-based ligands tend to produce more effective catalysts than cyclen-based ligands. Six of the eight catalysts identified as superior (red in Table 5) have cyclam ligands. Part of the reason may simply be stability, as we demonstrated that cyclam ligands were clearly superior to cyclen ligands in kinetic stability under harsh acidic

conditions. For reference, the last column of Table 5 shows the stability data for the copper complexes with these ligands. Clearly, there is some loose correlation between stability and catalytic efficiency. However, these dye-bleaching experiments were performed at pH = 7, so it is likely that acid-promoted ligand dissociation is not a significant concern here. From structural information gleaned from a vast number of crystal structures of ethylene cross-bridge tetraazamacrocyclic complexes reported in the Cambridge Structural Database (CSD) [51], the cyclam ligands provide a much better complementarity match (size, geometry, and electronics matching between ligand and metal) for first row transition metal ions. Therefore, the less distorted, and likely better orbital-overlapped, M-N bonds may simply lead to more reactive, or more robust, catalysts under these oxidizing conditions. Mn and Fe complexes in water with oxidizers such as H₂O₂ generally form insoluble oxides, a thermodynamic sink that leads to inactivation of many aqueous catalysts. Such a mechanism is avoided here due to the cross-bridged ligand stabilization of the complexes for both cyclam and cyclen complexes.

Observation 3: As demonstrated in the cyclic voltammetry experiments, higher oxidation potentials for the Fe³⁺ and Mn⁴⁺ species appear to lead to more efficient catalysis. Most obviously, the Fe complexes cannot achieve the +4 state and the associated high oxidation potential that this would require and are as such clearly inferior catalysts as a group. Conversely, all of the Mn complexes that were examined in MeCN can reversibly obtain the Mn⁴⁺ oxidation state and generally are more efficient catalysts. It is telling that the two top catalysts (ranked by “average rank ordering” each dye TOF among the top eight identified catalysts) are Mn⁴⁺-obtaining catalysts with observed oxidation potentials above 1.4 V: [MnL12Cl₂] at +1.433 V and [MnL8Cl₂] at 1.404 V. The other “top” Mn catalysts all achieve the Mn⁴⁺ oxidation state at or above 1.338 V. Clearly, catalysts that can achieve higher oxidation potentials are more active in the dye-bleaching tests we carried out. Interestingly, [MnL10Cl₂] ranks only “6”, even though its oxidation potential is 1.422 V. Thus, there are more factors at play here, even though oxidation potential appears to be a primary selector for high activity.

Observation 4: The three highest efficiency Mn catalysts all have a single benzyl pendant arm and either an allyl or methyl second pendant arm. This combination seems to provide the kinetic stability and oxidation potential for an efficient Mn catalyst. Perhaps the benzyl’s hydrophobicity may also be important in allowing good interaction with the organic substrate dyes, all of which contain multiple aromatic groups (Scheme 4). We targeted benzyl pendant arms as possible copolymerization groups using Friedel–Crafts polymerization [36] reactions and have begun to work towards producing such copolymers containing these monomeric catalysts as potential heterogeneous water purification materials.

Future work will need to build off the spectroscopic tracking of dye-bleaching work and what has been learned, namely, that Mn cyclam complexes with high oxidation potentials are the most efficient catalyst. We will need to begin to incorporate other substrates besides dyes, which are straightforward to track spectroscopically but not the only type of contaminant of emerging concern [62]. Antimicrobials and antibiotics are increasingly concerning to health officials as contaminants in waste water [63,64] and will thus be future substrates for our catalysts to be tested against. We will incorporate mass spectra tracking of aliquots over time to help determine rate as well as to gain information on potential mechanisms and products formed [65–67].

3. Experimental

3.1. General

All reagents and solvents were purchased from commercial sources and used as received. All solvents were of reagent grade and anhydrous. Electrospray mass spectra were recorded on a Shimadzu LCMS 2020 Electrospray Mass Spectrometer (Shimadzu, Kyoto, Japan). NMR spectra were collected on a Varian Bruker AVANCE II 300 MHz NMR Spectrometer instrument (Varian Bruker, Billerica, MA, USA). Electrochemical experiments

were completed on a BAS100B Electrochemical Analyzer (BASi, West Lafayette, IN, USA) at a scan rate of 200 mV/s under nitrogen atmosphere. A button Pt electrode, a Pt-wire electrode, and a Ag-wire electrode were used as working electrode, counter electrode, and pseudo-reference electrode, respectively. Acetonitrile solutions of the complexes (1 mM) with tetrabutylammonium hexafluorophosphate (0.1 M) were used as a supporting electrolyte. SHE using ferrocene (+0.400 V versus SHE) or acetylferrocene (+0.680 V versus SHE) was used as an internal standard for the measurements.

3.2. Synthesis

Ligands **L1** [45], **L2** [45], **L5** [45], **L6** [45], **L7** [33], and **L8** [32] were synthesized by literature procedures. **MnL1Cl₂**, **FeL1Cl₂**, **MnL2Cl₂**, **FeL2Cl₂**, **MnL5Cl₂**, **FeL5Cl₂**, **MnL6Cl₂**, **FeL6Cl₂** [13], and **FeL8Cl₂** [46] were prepared as previously published. Copper complexes were used only for kinetic decomplexation studies, for which the copper complexes of **L1**, **L2**, **L5**, and **L6** have already been published (see references in Table 3). **[CuL11Cl][PF₆]** and **[CuL12Cl][PF₆]** complexation never produced complexes with acceptable elemental analyses and are therefore not included in this study.

3.2.1. Synthesis of Novel Ligands and Precursors

Synthesis of 3. A total of 15.606 g (0.0464 mol, 1 eq) of the mono-methylated cyclen-glyoxal condensate **1** [47,48] was suspended in 400 mL of CH₃CN in a 1 L RB flask. Then, 34.70 mL of allyl bromide (56.16 g, 0.464 mol, 10 eq) was added and the reaction was stopped and stirred at room temperature for seven days. The product was filtered and washed (several times) with CH₃CN and ether and subsequently dried under vacuum, yielding 17.879 g (94%) of **3**. Elemental Analysis (%): calc C₁₄H₂₆N₄Br₂ · 0.9 H₂O (426.41 g/mol): C 39.43, H 6.57, N 13.14; Found C 39.66, H 6.20, N 13.16. MS (ES) *m/z* = 125 (L-2Br⁻)²⁺.

Synthesis of 4. A total of 9.935 g (0.0273 mol, 1 eq) of the mono-methylated cyclam-glyoxal condensate **2** [48] was suspended in 625 mL of CH₃CN in a 1 L RB flask. Then, 39.27 mL of allyl bromide (49.62 g, 0.410 mol, 15 eq) was added and the reaction was refluxed for 14 days under a nitrogen atmosphere using a water condenser and heating mantle. After the reaction was cooled to room temperature, the white solid product was filtered off using a glass frit then washed with CH₃CN and ether and dried under vacuum, yielding 11.058 g (92%) of **4**. Elemental Analysis (%): calc C₁₆H₃₀N₄Br₂ · 1.3 H₂O (461.67 g/mol): C 41.63, H 7.12, N 12.14; Found C 41.90, H 7.49, N 12.16. MS (ES) *m/z* = 139 (L-2Br⁻)²⁺.

Synthesis of L3. A total of 17.879 g (0.0436 mol, 1 eq) of **3** was stirred into 1500 mL of 95% EtOH in a 2 L RB flask. Then, 16.494 g (0.436 mol, 10 eq) of NaBH₄ was slowly added to the reaction at room temperature and stirred under a nitrogen atmosphere for five days. Next, 6 M HCl was added slowly to the RB flask until the solution reached a pH of 2. Ethanol was evaporated off using a rotary evaporator. Next, the product was dissolved in 200 mL of 30% KOH solution and extracted with 5 × 175 mL fractions of benzene using a separatory funnel. The benzene layer was collected and dried with sodium sulfate overnight. The sodium sulfate was filtered off and the remaining solvent evaporated to give a pale yellow oily product, which was dried under vacuum to yield 8.808 g (80%) of **L3**. Elemental Analysis (%): calc C₁₄H₂₈N₄ · 0.4 H₂O (259.61 g/mol): C 64.77, H 11.18, N 21.58; Found C 64.82, H 11.48, N 21.63. MS (ES) *m/z* = 253 (LH)⁺.

Synthesis of L4. A total of 11.653 g (0.0266 mol, 1 eq) of **4** was stirred into 860 mL of 95% EtOH in a 2 L RB flask. Then, 10.059 g (0.266 mol, 10 eq) of NaBH₄ was slowly added to the reaction at room temperature and stirred under nitrogen atmosphere for five days. Next, 6 M HCl was added slowly to the RB flask until the solution reached a pH of 2. Ethanol was evaporated off using a rotary evaporator. Next, the product was dissolved in 200 mL of 30% KOH solution and extracted with 3 × 175 mL fractions of benzene using a separatory funnel. The benzene layer was collected and dried with sodium sulfate overnight. The sodium sulfate was filtered off and the remaining solvent evaporated to give a pale yellow oily product, which was dried under vacuum to yield 4.132 g (55%) of

L5. Elemental Analysis (%): calc $C_{16}H_{32}N_4 \cdot 0.6 H_2O$ (291.26 g/mol): C 65.98, H 11.49, N 19.24; Found C 65.87, H 11.35, N 19.30. MS (ES) $m/z = 281$ (LH)⁺.

Synthesis of **7**. A total of 10.200 g (0.0592 mol, 1 eq) of **5** [48] was added to a 500 mL RB flask and dissolved in 100 mL of MeCN. Then, 71.384 g (50.99 mL, 0.592 mol, 10 eq) of allyl bromide was added, and the reaction was stoppered and stirred for five days. The white solid product was collected by filtration, washed with MeCN and ether, and dried under vacuum to yield 20.200 g (78%) of **7**. Elemental Analysis (%): calc $C_{16}H_{28}N_4Br \cdot 0.5 H_2O$ (445.24 g/mol): C 43.16, H 6.57, N 12.58; Found C 43.37, H 6.72, N 12.61. MS (ES) $m/z = 139$ (L-2Br)²⁺.

Synthesis of **8**. A total of 7.214 g (0.0360 mol, 1 eq) of **6** [48] was added to a 500 mL RB flask and dissolved in 100 mL of MeCN. Then, 39.201 g (28.00 mL, 0.360 mol, 10 eq) of allyl bromide was added, and the reaction was stoppered and stirred for seven days. The white solid product was collected by filtration, washed with MeCN and ether, and dried under vacuum to yield 13.528 g (81%) of **7**. Elemental Analysis (%): calc $C_{16}H_{28}N_4Br \cdot 1.0 CH_3CN \cdot 0.75 H_2O$ (518.85 g/mol): C 46.30, H 7.09, N 13.50; Found C 46.52, H 7.18, N 13.11. MS (ES) $m/z = 152$ (L-2Br)²⁺.

Synthesis of **L9**. A total of 20.201 g (0.0463 mol, 1 eq) of **7** was suspended in 1500 mL of 95% ethanol in a 2 L RB flask. Then, 17.515 g of sodium borohydride was slowly added to it over 10 min, and the reaction was stirred under nitrogen for seven days. Next, 6 M HCl was added to the reaction until the solution reached a pH of 2. The ethanol was evaporated, and the white residue was then dissolved into 50 mL of DI H₂O. Following this, 150 mL of 30% KOH solution was added, and the pH of the solution reached 14. Extraction was carried out with 4 × 100 mL fractions of benzene. The benzene layers were collected and dried over Na₂SO₄ overnight. After filtration of sodium sulfate, benzene was evaporated to give the pale yellow oily product, which was dried under vacuum to yield 8.555 g (66%) of **L9**. Elemental Analysis (%): calc $C_{16}H_{30}N_4 \cdot 0.4 H_2O$ (285.65 g/mol): C 67.28, H 10.87, N 19.61; Found C 67.03, H 10.69, N 19.90. MS (ES) $m/z = 279$ (LH)⁺.

Synthesis of **L10**. A total of 13.50 g (0.0291 mol, 1 eq) of **8** was suspended in 1500 mL of 95% EtOH in a 2 L RB flask. Then, 10.999 g (0.291 mol, 10 eq) of sodium borohydride was added, and the reaction mixture was stirred under nitrogen atmosphere for five days. Next, 6 M HCl solution was added until the pH reached 2. The ethanol was evaporated, and the residual white solid was dissolved in 50 mL DI water followed by addition of 250 mL of 30% KOH solution. Extraction was carried out with 4 × 100 mL fractions of benzene. The benzene layers were collected and dried over Na₂SO₄ overnight. After filtration of sodium sulfate, benzene was evaporated to give the pale yellow oily product, which was dried under vacuum to yield 5.124 g (57%) of **L10**. Elemental Analysis (%): calc $C_{18}H_{34}N_4$ (285.65 g/mol): C 70.54, H 11.18, N 18.28; Found C 70.50, H 11.64, N 18.38. MS (ES) $m/z = 307$ (LH)⁺.

Synthesis of **11**. A total of 22.065 g (0.0604 mol, 1 eq) of **9** [48] was suspended in 300 mL of acetonitrile. Then, 73.072 g (0.604 mol, 10 eq) of allyl bromide was added, and the reaction was stoppered and stirred for three days. The white solid product was collected by filtration, washed with MeCN and ether, and dried under vacuum to yield 24.301 g (83%) of **9**. Elemental Analysis (%): calc $C_{20}H_{30}N_4Br_2 \cdot 2.0 H_2O$ (522.33 g/mol): C 45.99, H 6.56, N 10.73; Found C 45.85, H 6.39, N 10.72. MS (ES) $m/z = 407$ (L-Br)⁺; $m/z = 163$ (L-2Br)²⁺.

Synthesis of **12**. A total of 4.379 g (0.0111 mol, 1 eq) of **10** [48] was suspended in 50 mL of acetonitrile. Then, 13.429 g (0.111 mol, 10 eq) of allyl bromide was added, and the reaction was stoppered and stirred for three days. The white solid product was collected by filtration, washed with MeCN and ether, and dried under vacuum to yield 1.835 g (32%) of **12**. Elemental Analysis (%): calc $C_{22}H_{34}N_4Br_2 \cdot 1.3 H_2O$ (537.77 g/mol): C 45.14, H 6.86, N 10.42; Found C 49.35, H 6.94, N 10.11. MS (ES) $m/z = 433$ (L-Br)⁺.

Synthesis of **L11**. A total of 14.591 g (0.0300 mol, 1 eq) of **11** was suspended in 1000 mL of 95% ethanol in an RB flask. Then, 11.351 g (0.300 mol, 10 eq) of sodium borohydride was slowly added to it over 10 min, and the reaction was stirred under nitrogen for nine days. Next, 6 M HCl was added to the reaction until the solution reached a pH of 2.

The ethanol was evaporated, and the white residue was then dissolved into 50 mL of DI H₂O. Following this, 200 mL of 30% KOH solution was added, and the pH of the solution reached 14. Extraction was carried out with 5 × 175 mL fractions of benzene. The benzene layers were collected and dried over Na₂SO₄ overnight. After filtration of sodium sulfate, benzene was evaporated to give the pale yellow oily product, which was dried under vacuum to yield 6.432 g (65%) of **L11**. Elemental Analysis (%): calc C₂₀H₃₂N₄ · 0.1 C₆H₆ · 1.6 H₂O (365.13 g/mol): C 67.76, H 9.88, N 15.34; Found C 67.61, H 9.69, N 14.99. MS (ES) *m/z* = 329 (LH)⁺.

Synthesis of **L12**. A total of 9.243 g (0.0180 mol, 1 eq) of **12** was suspended in 1000 mL of 95% ethanol in a 2 L RB flask. Then, 6.798 g (0.180 mol, 10 eq) of sodium borohydride was slowly added to it over 10 min, and the reaction was stirred under nitrogen for eight days. Next, 6 M HCl was added to the reaction until the solution reached a pH of 2. The ethanol was evaporated, and the white residue was then dissolved into 50 mL of DI H₂O. Following this, 200 mL of 30% KOH solution was added, and the pH of the solution reached 14. Extraction was carried out with 5 × 175 mL fractions of benzene. The benzene layers were collected and dried over Na₂SO₄ overnight. After filtration of sodium sulfate, benzene was evaporated to give the pale yellow oily product, which was dried under vacuum to yield 6.044 g (94%) of **L12**. Elemental Analysis (%): calc C₂₂H₃₆N₄ · 1.2 H₂O (378.17 g/mol): C 69.87, H 10.23, N 14.82; Found C 69.79, H 9.84, N 15.11. MS (ES) *m/z* = 357 (LH)⁺.

3.2.2. Synthesis of Novel Metal Complexes

General Procedure for Complexation of CuCl₂, MnCl₂, or FeCl₂

In an inert atmosphere glove box, 0.001 mol of ligand and 0.001 mol of anhydrous MCl₂ were stirred in 15 mL anhydrous aprotic solvent if M = Fe/Mn (either MeCN, DMF), or MeOH if M = Cu, for 24 h. Products, blue (Cu), white (Mn), or light brown (Fe), may precipitate and be filtered from the reaction solution (Fraction A) and be washed with MeCN and allowed to air dry in the glovebox. Alternatively, products may remain soluble in the reaction mixture (Fraction B). For “Fraction B” complexes, 200 mL of anhydrous ether were added to the filtrate, which resulted in the precipitation of the product, which was collected on a fine frit, washed with ether, allowed to dry while it was open to the glovebox atmosphere, and then scraped from the frit with a spatula into a vial for storage. For Cu, “Fraction C” complexes were necessary in some cases to achieve pure products: the reaction mixture was removed from the glovebox, filtered to remove trace solids, and evaporated to dryness. The residue was then dissolved in a minimum of methanol, and a methanol solution of 5 eq of NH₄PF₆ was added to precipitate the blue solid products, which were filtered off, washed with methanol and ether, and dried under vacuum.

[CuL3Cl₂]: MeCN. Fraction B. Yield: 0.213 g (55%). Elemental Analysis (%): calc [Cu(C₁₄H₂₈N₄)Cl₂] · 1.5 H₂O (386.85 g/mol): C 40.63, H 7.55, N 13.54; Found C 40.86, H 7.21, N 13.70. MS (ES) *m/z* = 352 (CuLCl)⁺.

MnL3Cl₂: MeCN. Fraction B. Yield: 0.172 g (45%). Elemental Analysis (%): calc [Mn(C₁₄H₂₈N₄)Cl₂] · 0.8 H₂O (392.66 g/mol): C 42.82, H 7.60, N 14.27; Found C 42.82, H 7.44, N 14.39. MS (ES) *m/z* = 342 (MnLCl)⁺.

FeL3Cl₂: MeCN. Fraction B. Yield: 0.157 g (41%). Elemental Analysis (%): calc [Fe(C₁₄H₂₈N₄)Cl₂] · 0.3 H₂O (384.55 g/mol): C 43.73, H 7.50, N 14.57; Found C 43.63, H 7.58, N 14.55. MS (ES) *m/z* = 343 (FeLCl)⁺.

[CuL4Cl][PF₆]: MeCN. Fraction C. Yield: 0.286 g (49%). Elemental Analysis (%): calc [Cu(C₁₆H₃₂N₄)Cl_{0.5}][PF₆]_{1.5} (579.18 g/mol): C 33.18, H 5.57, N 9.67; Found C 33.15, H 5.62, N 9.65. MS (ES) *m/z* = 379 (CuLCl)⁺.

MnL4Cl₂: MeCN. Fraction B. Yield: 0.185 g (45%). Elemental Analysis (%): calc [Mn(C₁₆H₃₂N₄)Cl₂] · 1.0 H₂O (424.31 g/mol): C 45.29, H 8.08, N 13.20; Found C 45.18, H 8.00, N 13.37. MS (ES) *m/z* = 370 (MnLCl)⁺.

FeL4Cl₂: MeCN. Fraction B. Yield: 0.163 g (40%). Elemental Analysis (%): calc [Fe(C₁₆H₃₂N₄)Cl₂] · 1.5 H₂O (424.31 g/mol): C 44.26, H 8.12, N 12.90; Found C 43.87, H 7.66, N 13.27. MS (ES) *m/z* = 371 (FeLCl)⁺.

[CuL7Cl][PF₆]: MeOH. Fraction B. Yield: 0.289 g (79%). Elemental Analysis (%): calc [Cu(C₁₈H₃₀N₄)Cl][PF₆] · 2.5 H₂O (481.95 g/mol): C 44.86, H 7.32, N 11.63; Found C 44.51, H 7.26, N 11.89. MS (ES) *m/z* = 400 (CuLCl)⁺.

MnL7Cl₂: DMF. Fraction A. Yield: 0.295 g (69%). Elemental Analysis (%): calc [Mn(C₁₈H₃₀N₄)Cl₂] (428.30 g/mol): C 50.48, H 7.06, N 13.08; Found C 50.38, H 7.24, N 12.92. MS (ES) *m/z* = 393 (MnLCl)⁺.

FeL7Cl₂: DMF. Fraction A. Yield: 0.308 g (72%). Elemental Analysis (%): calc [Mn(C₁₈H₃₀N₄)Cl₂] · 1.0 DMF · 1.0 H₂O (511.31 g/mol): C 49.33, H 7.49, N 13.70; Found C 49.41, H 7.66, N 13.53. MS (ES) *m/z* = 394 (FeLCl)⁺.

[CuL8Cl]PF₆: MeOH. Fraction C. Yield: 0.523 g (84%). Elemental Analysis (%): calc [Cu(C₂₀H₃₄N₄)Cl][PF₆] · 0.3 NH₄PF₆ (623.38 g/mol): C 38.54, H 5.69, N 9.66; Found C 38.22, H 5.75, N 9.72. MS (ES) *m/z* = 428 (CuLCl)⁺.

[CuL9Cl]PF₆: MeOH. Fraction C. Yield: 0.169 g (31%). Elemental Analysis (%): calc [Cu(C₁₆H₃₀N₄)Cl][PF₆] · 1.0 H₂O (540.41 g/mol): C 35.56, H 5.97, N 10.37; Found C 35.67, H 5.84, N 10.57. MS (ES) *m/z* = 376 (CuLCl)⁺.

MnL9Cl₂: MeCN. Fraction B. Yield: 0.238 g (59%). Elemental Analysis (%): calc [Mn(C₁₆H₃₀N₄)Cl₂] · 0.5 H₂O (413.29 g/mol): C 46.50, H 7.56, N 13.56; Found C 46.73, H 7.69, N 13.85. MS (ES) *m/z* = 369 (MnLCl)⁺.

FeL9Cl₂: MeCN. Fraction B. Yield: 0.188 g (46%). Elemental Analysis (%): calc [Fe(C₁₆H₃₀N₄)Cl₂] · 0.5 H₂O (414.19 g/mol): C 46.40, H 7.54, N 13.53; Found C 46.33, H 7.63, N 13.58. MS (ES) *m/z* = 370 (FeLCl)⁺.

[CuL10Cl][PF₆]: MeOH. Fraction C. Yield: 0.226 g (41%). Elemental Analysis (%): calc [Cu(C₁₈H₃₄N₄)Cl][PF₆] · 1.5 H₂O (540.41 g/mol): C 37.44, H 6.46, N 9.70; Found C 37.52, H 6.11, N 9.43. MS (ES) *m/z* = 404 (CuLCl)⁺.

MnL10Cl₂: MeCN. Fraction B. Yield: 0.217 g (50%). Elemental Analysis (%): calc [Mn(C₁₈H₃₄N₄)Cl₂] · 1.0 H₂O (450.35 g/mol): C 48.01, H 8.06, N 12.44; Found C 48.30, H 8.31, N 12.45. MS (ES) *m/z* = 397 (MnLCl)⁺.

FeL10Cl₂: MeCN. Fraction B. Yield: 0.195 g (45%). Elemental Analysis (%): calc [Fe(C₁₈H₃₄N₄)Cl₂] · 1.5 H₂O (460.26 g/mol): C 46.97, H 8.10, N 12.17; Found C 46.93, H 7.98, N 12.06. MS (ES) *m/z* = 398 (FeLCl)⁺.

MnL11Cl₂: MeCN. Fraction B. Yield: 0.253 g (56%). Elemental Analysis (%): calc [Mn(C₂₀H₃₂N₄)Cl₂] · 0.5 H₂O (424.31 g/mol): C 51.84, H 7.18, N 12.09; Found C 51.59, H 7.19, N 11.94. MS (ES) *m/z* = 419 (MnLCl)⁺.

FeL11Cl₂: MeCN. Fraction B. Yield: 0.386 g (85%). Elemental Analysis (%): calc [Fe(C₂₀H₃₂N₄)Cl₂] · 3.5 H₂O (518.30 g/mol): C 46.35, H 7.58, N 10.81; Found C 46.64, H 7.24, N 10.50. MS (ES) *m/z* = 420 (FeLCl)⁺.

MnL12Cl₂: MeCN. Fraction A. Yield: 0.147 g (30%). Elemental Analysis (%): calc [Mn(C₂₂H₃₆N₄)Cl₂] · 0.3 H₂O (487.80 g/mol): C 54.17, H 7.56, N 11.49; Found C 54.02, H 7.55, N 11.50. MS (ES) *m/z* = 446 (MnLCl)⁺.

FeL12Cl₂: MeCN. Fraction A. Yield: 0.162 g (34%). Elemental Analysis (%): calc [Fe(C₂₂H₃₆N₄)Cl₂] · 0.6 H₂O (494.11 g/mol): C 53.48, H 7.59, N 11.34; Found C 53.21, H 7.55, N 11.35. MS (ES) *m/z* = 447 (FeLCl)⁺.

3.3. Characterization

3.3.1. Acid Decomplexation Studies

This experiment is a typical technique for comparing the kinetic stability of new cross-bridged ligands [21–23,31,49,52–54]. The d-d absorption band (generally near 600 nm) of the respective copper complexes (1 mM concentration) was studied on a Shimadzu UV-3600 spectrophotometer (Shimadzu, Kyoto, Japan) in the presence of acidic solutions of varying concentration. The decomposition behaviors of the different copper complexes in acidic conditions were monitored at increasing temperatures until they decomposed (in a matter of hours/days). As the absorption decreased over time, appearance of an isosbestic point on each spectrum confirmed the presence of a single decomposition product, likely CuCl_{2(aq)}. The decomposition of copper complexes followed pseudo-first-order kinetics.

The half-lives of the respective complexes were calculated from the plot of \ln absorbance (absorbance at maxima of the spectra) vs. time.

3.3.2. X-ray Crystallography Studies

The crystal structure data for all of the metal complexes were collected using a Bruker diffractometer employing Mo K α radiation ($\lambda = 0.71073 \text{ \AA}$), a TRIUMPH curved-graphite monochromator, and either an APEX-II or PHOTON-II detector. Data were corrected for the effects of absorption using a multi-scan method within SADABS. The sample was held at 120 K in an Oxford Cryosystems nitrogen gas cryostream.

L8 precursor: Data were collected through the SCrALS (Service Crystallography at the Advanced Light Source) program at Beamline 11.3.1 at the Advanced Light Source (ALS), Lawrence Berkeley National Laboratory. The instrument employed is based on a commercial Bruker diffractometer with a PHOTON 100 detector and an operating wavelength of 0.7749 \AA . The data were corrected for the effects of beam decay and absorption using SADABS. The sample was held at 150 K in an Oxford Cryosystems nitrogen gas cryostream.

CCDC-2268469-2268475 contain the supplementary crystallographic data (Tables S1–S52) for this paper. These data can be obtained free of charge from The Cambridge Crystallographic Data Centre via www.ccdc.cam.ac.uk/data_request/cif.

3.4. Dye-Bleaching Studies

All of the dye-decolorization studies were performed in water at pH 7, following the procedure of Yin et al. [68]. The three dyes, methylene blue (MB), methylene orange (MO), and Rhodamine B (RhB), had concentrations of 3.35 mM, 3.83 mM, and 2.60 mM, respectively, whereas the metal complex stock solutions had a 1.00 mM concentration. For each experiment, 10.00 mL of dye solution was added to 10.00 mL of metal complex stock solution. pH was kept neutral with the usage of either 0.100 M HCl or 0.100 M NaOH. Further, water was added to each set to adjust the volume up to 25 mL. Accordingly, the final concentrations of the metal complex and three dyes, namely, MB, MO, and RhB, were calculated to be 0.40 mM, 1.34 mM, 1.53 mM, and 1.04 mM, respectively. For these studies, 0.25 mL of 30% H₂O₂ was added to each set to trigger the dye-bleaching process. To monitor the progress of the reaction, 1 mL reaction mixture aliquots were taken out at certain time intervals. After removal, each aliquot set was diluted to 100 mL with water in order to quench the bleaching reaction. Next, absorbance spectra were recorded, and the absorbance maxima values at 664 nm, 465 nm and 553 nm were monitored for reaction mixture containing MB, MO, and, RhB, respectively. Time zero was defined as the time of H₂O₂ addition. Further, the absorbance was monitored at 5, 10, 20, 30, 60, 120, 180, 240, 300 min, or more (until the dye reached ~10% of its actual absorbance). For each set, at least two trials were performed, and all the absorbance values reported are an average value of the trials.

4. Conclusions

Potentially copolymerizable allyl and benzyl pendant-armed ethylene cross-bridged tetraazamacrocycles were synthesized, and twenty of their novel Mn, Fe, and Cu complexes were produced and characterized. Two cis coordination sites are available for interaction with substrate and oxidant due to the cis-folded pseudo-octahedral geometry forced by the rigidifying ethylene cross-bridge, as demonstrated by multiple X-ray crystal structures. The cyclam-based ligands, in particular, provide superior stabilization with half-lives of the Cu complexes of many minutes or even hours in 5 M HCl at 50–90 °C, as determined by kinetic stability experiments under harsh acidic and high-temperature conditions. Reversible redox processes indicated stabilization of Fe²⁺/Fe³⁺ and Mn²⁺/Mn³⁺/Mn⁴⁺ oxidation states, supporting the likelihood of catalytic oxidation for these complexes. Finally, Mn cross-bridged cyclam complexes with at least one benzyl pendant arm performed best in dye-bleaching experiments with methylene blue, methyl orange, and rhodamine B. Future

work will include selection of the most successful monomeric catalysts for copolymerization to produce future heterogeneous water purification materials.

Supplementary Materials: The following supporting information can be downloaded at: <https://www.mdpi.com/article/10.3390/molecules28186466/s1>. Figures S1–S12: ^1H and ^{13}C NMR spectra for novel organic compounds. Figure S13: Example of kinetic decomplexation plot to determine $t_{1/2}$ for copper complexes. Figures S14–S21: Cyclic voltammograms for novel Mn and Fe complexes. Figures S22–S33: Dye bleaching plots of catalyst, H_2O_2 , and dye (MB, MO, RhB). Tables S1–S52: Crystallographic details for all new structures [69–71].

Author Contributions: Conceptualization, T.J.H.; methodology, T.J.H., L.G. and M.R.K. validation, L.G. and M.R.K.; formal analysis, T.J.H., S.M., J.A.K., A.G.O. and T.J.P.; investigation, T.J.H., M.R.K., L.G., J.T.P., W.A.T., E.M.A.A., A.G.M., D.J.C.-S., N.L.F., T.H., I.K., D.J.H., J.A.K., A.G.O. and T.J.P.; resources, T.J.H., J.A.K., A.G.O. and T.J.P.; data curation, T.J.H., S.M., J.A.K., A.G.O. and T.J.P.; writing—original draft preparation, S.M., T.J.H. and T.J.P.; writing—review and editing, T.J.H., J.A.K., A.G.O. and T.J.P.; visualization, T.J.H., S.M. and T.J.P.; supervision, T.J.H.; project administration, T.J.H.; funding acquisition, T.J.H., J.A.K. and A.G.O. All authors have read and agreed to the published version of the manuscript.

Funding: This material is based on work supported by the National Science Foundation under Grant No. OIA-1946093. Any opinions, findings, conclusions, or recommendations expressed in this material are those of the author(s) and do not necessarily reflect the views of the National Science Foundation. Acknowledgement is made to the donors of the American Chemical Society Petroleum Research Fund for partial support of this work. T.J.H., E.M.A.A., A.G.M., D.J.C.-S. and L.G. also acknowledge OK-LSAMP and NSF for support.

Data Availability Statement: Data presented in this study are available in the Supplementary Materials or upon request from the corresponding authors.

Acknowledgments: Samples for synchrotron crystallographic analysis were submitted through the SCrALS (Service Crystallography at Advanced Light Source) program. Crystallographic data were collected at Beamline 11.3.1 at the Advanced Light Source (ALS), Lawrence Berkeley National Laboratory. The ALS is supported by the U.S. Department of Energy, Office of Energy Sciences, under contract DE-AC02-05CH11231.

Conflicts of Interest: The authors declare no conflict of interest.

Sample Availability: Samples of the compounds are not available.

References

1. Schäfer, F.P.; Schmidt, W.; Volze, J. Organic dye solution laser. *Appl. Phys. Lett.* **1966**, *9*, 306–309. [[CrossRef](#)]
2. Mustroph, H.; Stollenwerk, M.; Bressau, V. Current Developments in Optical Data Storage with Organic Dyes. *Angew. Chem.* **2006**, *45*, 2016–2035. [[CrossRef](#)]
3. Chiu, Y.-H.; Chang, T.-F.M.; Chen, C.-Y.; Sone, M.; Hsu, Y.-J. Mechanistic Insights into Photodegradation of Organic Dyes Using Heterostructure Photocatalysts. *Catalysts* **2019**, *9*, 430. [[CrossRef](#)]
4. Tkaczyk, A.; Mitrowska, K.; Posyniak, A. Synthetic organic dyes as contaminants of the aquatic environment and their implications for ecosystems: A review. *Sci. Total. Environ.* **2020**, *717*, 137–222. [[CrossRef](#)]
5. Epling, G.A.; Lin, C. Photoassisted bleaching of dyes utilizing TiO_2 and visible light. *Chemosphere* **2002**, *46*, 561–570. [[CrossRef](#)] [[PubMed](#)]
6. Wang, Z.; Yuan, R.; Guo, Y.; Xu, L.; Liu, J. Effects of chloride ions on bleaching of azo dyes by Co^{2+} /oxone reagent: Kinetic analysis. *J. Hazard. Mater.* **2011**, *190*, 1083–1087. [[CrossRef](#)] [[PubMed](#)]
7. Zucca, P.; Neves, C.M.B.; Simões, M.M.Q.; Neves, M.D.G.P.M.S.; Cocco, G.S.; Sanjust, E. Immobilized Lignin Peroxidase-Like Metalloporphyrins as Reusable Catalysts in Oxidative Bleaching of Industrial Dyes. *Molecules* **2016**, *21*, 964. [[CrossRef](#)]
8. Santos, M.C.; Antonin, V.S.; Souza, F.M.; Aveiro, L.R.; Pinheiro, V.S.; Gentil, T.C.; Lima, T.S.; Moura, J.P.C.; Silva, C.R.; Lucchetti, L.E.B.; et al. Decontamination of wastewater containing contaminants of emerging concern by electrooxidation and Fenton-based processes—A review on the relevance of materials and methods. *Chemosphere* **2022**, *307*, 135763. [[CrossRef](#)]
9. Kiselev, V.M.; Evstrop'ev, S.K.; Starodubtsev, A.M. Photocatalytic degradation and sorption of methylene blue on the surface of metal oxides in aqueous solutions of the dye. *Opt. Spectrosc.* **2017**, *123*, 809–815. [[CrossRef](#)]
10. da Rocha, M.G.; Nakagaki, S.; Ucoski, G.M.; Wypych, F.; Machado, G.S. Comparison between catalytic activities of two zinc layered hydroxide salts in brilliant green organic dye bleaching. *J. Colloid Interface Sci.* **2019**, *541*, 425–433. [[CrossRef](#)]

11. Zhang, Y.H.G.; Zhang, G. A novel mixed-phase TiO₂/kaolinite composites and their photocatalytic activity for degradation of organic contaminants. *Chem. Eng. J.* **2011**, *172*, 936–943. [[CrossRef](#)]
12. Hubin, T.J.; McCormick, J.M.; Collinson, S.R.; Buchalova, M.; Perkins, C.M.; Alcock, N.W.; Kahol, P.K.; Raghunathan, A.; Busch, D.H. New iron(II) and manganese(II) complexes of two ultra-rigid, cross-bridged tetraazamacrocycles for catalysis and biomimicry. *J. Am. Chem. Soc.* **2000**, *122*, 2512–2522. [[CrossRef](#)]
13. Hubin, T.J.; McCormick, J.M.; Collinson, S.R.; Alcock, N.W.; Clase, H.J.; Busch, D.H. Synthesis and X-ray crystal structures of iron(II) and manganese(II) complexes of unsubstituted and benzyl substituted cross-bridged tetraazamacrocycles. *Inorg. Chim. Acta* **2003**, *346*, 76–86. [[CrossRef](#)]
14. Busch, D.H.; Collinson, S.R.; Hubin, T. Catalysts and Methods for Catalytic Oxidation. U.S. Patent 6,906,189, 14 June 2005.
15. Yin, G.; Danby, A.M.; Kitko, D.; Carter, J.D.; Scheper, W.M.; Busch, D.H. Olefin Epoxidation by Alkyl Hydroperoxide with a Novel Cross-Bridged Cyclam Manganese Complex: Demonstration of Oxygenation by Two Distinct Reactive Intermediates. *Inorg. Chem.* **2007**, *46*, 2173–2180. [[CrossRef](#)] [[PubMed](#)]
16. Yin, G.C.; Danby, A.M.; Kitko, D.; Carter, J.D.; Scheper, W.M.; Busch, D.H. Oxidative reactivity difference among the metal oxo and metal hydroxo moieties: pH dependent hydrogen abstraction by a manganese(IV) complex having two hydroxide ligands. *J. Am. Chem. Soc.* **2008**, *130*, 16245–16253. [[CrossRef](#)] [[PubMed](#)]
17. Chattopadhyay, S.; Geiger, R.A.; Yin, G.; Busch, D.H.; Jackson, T.A. Oxo- and Hydroxomanganese(IV) Adducts: A Comparative Spectroscopic and Computational Study. *Inorg. Chem.* **2010**, *49*, 7530–7535. [[CrossRef](#)]
18. Dong, L.; Wang, Y.; Lu, Y.; Chen, Z.; Mei, F.; Xiong, H.; Yin, G. Lewis-Acid-Promoted Stoichiometric and Catalytic Oxidations by Manganese Complexes Having Cross-Bridged Cyclam Ligand: A Comprehensive Study. *Inorg. Chem.* **2013**, *52*, 5418–5427. [[CrossRef](#)]
19. Tan, P.; Kwong, H.-K.; Lau, T.-C. Catalytic oxidation of water and alcohols by a robust iron(III) complex bearing a cross-bridged cyclam ligand. *Chem. Commun.* **2015**, *51*, 12189–12192. [[CrossRef](#)]
20. Annunziata, A.; Esposito, R.; Gatto, G.; Cucciolo, M.E.; Tuzi, A.; Macchioni, A.; Ruffo, F. Iron(III) Complexes with Cross-Bridged Cyclams: Synthesis and Use in Alcohol and Water Oxidation Catalysis. *Eur. J. Inorg. Chem.* **2018**, *2018*, 3304–3311. [[CrossRef](#)]
21. Matz, D.L.; Jones, D.G.; Roewe, K.D.; Gorbet, M.J.; Zhang, Z.; Chen, Z.Q.; Prior, T.J.; Archibald, S.J.; Yin, G.C.; Hubin, T.J. Synthesis, structural studies, kinetic stability, and oxidation catalysis of the late first row transition metal complexes of 4,10-dimethyl-1,4,7,10-tetraazabicyclo [6.5.2]pentadecane. *Dalton Trans.* **2015**, *44*, 12210–12224. [[CrossRef](#)]
22. Jones, D.G.; Wilson, K.R.; Cannon-Smith, D.J.; Shircliff, A.D.; Zhang, Z.; Chen, Z.; Prior, T.J.; Yin, T.J.; Hubin, T.J. Synthesis, structural studies, and oxidation catalysis of the late-first-row-transition-metal complexes of a 2-pyridylmethyl pendant-armed ethylene cross-bridged cyclam. *Inorg. Chem.* **2015**, *54*, 2221–2234. [[CrossRef](#)] [[PubMed](#)]
23. Odendaal, A.Y.; Fiamengo, A.L.; Ferdani, R.; Wadas, T.J.; Hill, D.C.; Peng, Y.; Heroux, K.J.; Golen, J.A.; Rheingold, A.L.; Anderson, C.J.; et al. Isomeric Trimethylene and Ethylene Pendant-armed Cross-bridged Tetraazamacrocycles and in Vitro/in Vivo Comparisons of their Copper(II) Complexes. *Inorg. Chem.* **2011**, *50*, 3078–3086. [[CrossRef](#)] [[PubMed](#)]
24. Sun, X.; Wuest, M.; Weisman, G.R.; Wong, E.H.; Reed, D.P.; Boswell, C.A.; Motekaitis, R.; Martell, A.E.; Welch, M.J.; Anderson, C.J. Radiolabeling and in vivo behavior of copper-64-labeled cross-bridged cyclam ligands. *J. Med. Chem.* **2002**, *45*, 469–477. [[CrossRef](#)] [[PubMed](#)]
25. Boswell, C.A.; Sun, X.; Niu, W.; Weisman, G.R.; Wong, E.H.; Rheingold, A.L.; Anderson, C.J. Comparative in vivo stability of copper-64-labeled cross-bridged and conventional tetraazamacrocyclic complexes. *J. Med. Chem.* **2004**, *47*, 1465–1474. [[CrossRef](#)] [[PubMed](#)]
26. Heroux, K.J.; Woodin, K.S.; Tranchemontagne, D.J.; Widger, P.C.B.; Southwick, E.; Wong, E.H.; Weisman, G.R.; Tomellini, S.A.; Wadas, T.J.; Anderson, C.J.; et al. The long and short of it: The influence of N-carboxyethyl versus N-carboxymethyl pendant arms on in vitro and in vivo behavior of copper complexes of cross-bridged tetraamine macrocycles. *Dalton Trans.* **2007**, *21*, 2150–2162. [[CrossRef](#)]
27. Sprague, J.E.; Peng, Y.; Fiamengo, A.L.; Woodin, K.S.; Southwick, E.A.; Weisman, G.R.; Wong, E.H.; Golen, J.A.; Rheingold, A.L.; Anderson, C.J. Synthesis, Characterization and In Vivo Studies of Cu(II)-64-Labeled Cross-Bridged Tetraazamacrocycle-amide Complexes as Models of Peptide Conjugate Imaging Agents. *J. Med. Chem.* **2007**, *50*, 2527–2535. [[CrossRef](#)]
28. Anderson, C.J.; Wadas, T.J.; Wong, E.H.; Weisman, G.R. Cross-bridged Macrocyclic Chelators for Stable Complexation of Copper Radionuclides for PET Imaging. *Q. J. Nucl. Med. Mol. Imaging* **2008**, *52*, 185–192.
29. Ferdani, R.; Stigers, D.J.; Fiamengo, A.L.; Wei, L.; Li, B.T.Y.; Golen, J.A.; Rheingold, A.L.; Weisman, G.R.; Wong, E.H.; Anderson, C.J. Synthesis, Cu(II) complexation, ⁶⁴Cu-labeling and biological evaluation of cross-bridged cyclam chelators with phosphonate pendant arms. *Dalton Trans.* **2012**, *41*, 1938–1950. [[CrossRef](#)]
30. Burke, B.P.; Miranda, C.S.; Lee, R.E.; Renard, L.; Nigam, S.; Clemente, G.S.; D’Huys, T.; Ruest, T.; Domarkas, J.; Thompson, J.A.; et al. Cu PET Imaging of the CXCR4 Chemokine Receptor Using a Cross-Bridged Cyclam Bis-Tetraazamacrocyclic Antagonist. *J. Nucl. Med.* **2020**, *61*, 123–128. [[CrossRef](#)]
31. Wadas, T.J.; Wong, E.H.; Weisman, G.R.; Anderson, C.J. Coordinating Radiometals of Copper, Gallium, Indium, Yttrium, and Zirconium for PET and SPECT Imaging of Disease. *Chem. Rev.* **2010**, *110*, 2858–2902. [[CrossRef](#)]
32. Khan, A.; Nicholson, G.; Greenman, J.; Madden, L.; McRobbie, G.; Pannecouque, C.; De Clercq, E.; Ullom, R.; Maples, D.L.; Maples, R.D.; et al. Binding Optimization through Coordination Chemistry: CXCR4 Chemokine Receptor Antagonists from Ultrarigid Metal Complexes. *J. Am. Chem. Soc.* **2009**, *131*, 3416–3417. [[CrossRef](#)] [[PubMed](#)]

33. Maples, R.D.; Cain, A.N.; Burke, B.P.; Silversides, J.D.; Mewis, R.; D'huys, T.; Schols, D.; Linder, D.P.; Archibald, S.J.; Hubin, T.J. Aspartate-based CXCR4 chemokine receptor binding of cross-bridged tetraazamacrocyclic copper(II) and zinc(II) complexes. *Chem. A Eur. J.* **2016**, *22*, 12916–12930. [[CrossRef](#)] [[PubMed](#)]
34. Hoang, T.; Mondal, S.; Allen, M.B.; Garcia, L.; Krause, J.A.; Oliver, A.G.; Prior, T.J.; Hubin, T.J. Synthesis and Characterization of Late Transition Metal Complexes of Mono-Acetate Pendant Armed Ethylene Cross-Bridged Tetraazamacrocycles with Promise as Oxidation Catalysts for Dye Bleaching. *Molecules* **2023**, *28*, 232. [[CrossRef](#)] [[PubMed](#)]
35. Munnik, P.; De Jongh, P.E.; De Jong, K.P. Recent Developments in the Synthesis of Supported Catalysts. *Chem. Rev.* **2015**, *115*, 6687–6718. [[CrossRef](#)]
36. Ganesan, V.; Yoon, S. Direct Heterogenization of Salphen Coordination Complexes to Porous Organic Polymers: Catalysts for Ring-Expansion Carbonylation of Epoxides. *Inorg. Chem.* **2020**, *59*, 2881–2889. [[CrossRef](#)]
37. Huang, Y.; Liu, T.; Lin, J.; Lu, J.; Lin, Z.; Cao, R. Homochiral Nickel Coordination Polymers Based on Salen(Ni) Metalloligands: Synthesis, Structure, and Catalytic Alkene Epoxidation. *Inorg. Chem.* **2011**, *50*, 2191–2198. [[CrossRef](#)]
38. Yuan, G.; Jiang, H.; Zhang, L.; Liu, Y.; Cui, Y. Metallosalen-based crystalline porous materials: Synthesis and property. *Coord. Chem. Rev.* **2019**, *378*, 483–499. [[CrossRef](#)]
39. Liu, T.-T.; Liang, J.; Xu, R.; Huang, Y.-B.; Cao, R. Salen-Co(III) insertion in multivariate cationic metal-organic frameworks for the enhanced cycloaddition reaction of carbon dioxide. *Chem. Commun.* **2019**, *55*, 4063–4066. [[CrossRef](#)]
40. Tan, L.; Tan, B. Hypercrosslinked porous polymer materials: Design, synthesis, and applications. *Chem. Soc. Rev.* **2017**, *46*, 3322–3356. [[CrossRef](#)]
41. Friedel, C.; Crafts, J.M. Sur une nouvelle méthode générale de synthèse d'hydrocarbures, d'acétones, etc. *Compte. Rend.* **1877**, *84*, 1392.
42. Begni, F.; Gullo, F.; Paul, G.; Rea, R.; Ferrari, M.-C.; Mangano, E.; Cossi, M.; Gatti, G.; Marchese, L. Optimization of the Friedel–Crafts Alkylation for the Synthesis of Hyper-Cross-Linked Polymers. *ACS Appl. Polym. Mater.* **2022**, *4*, 5281–5286. [[CrossRef](#)]
43. Leeuwen, P.W.N.M. Alkene Polymerisation. In *Homogeneous Catalysis*, 1st ed.; Springer: Dordrecht, The Netherlands, 2004; pp. 191–228. [[CrossRef](#)]
44. Zuo, X.; Mosha, D.; Archibald, S.J.; McCasland, A.K.; Hassan, A.M.; Givens, R.S.; Busch, D.H. Towards the soil poultice and a new separations methodology: Rebinding of macrocyclic metal complexes to molecularly imprinted polymers specifically templated via noncovalent interactions. *J. Coord. Chem.* **2005**, *58*, 21–39. [[CrossRef](#)]
45. Weisman, G.R.; Wong, E.H.; Hill, D.C.; Rogers, M.E.; Reed, D.P.; Calabrese, J.C. Synthesis and transition-metal complexes of new cross-bridged tetraamine ligands. *Chem. Commun.* **1996**, *8*, 947–948. [[CrossRef](#)]
46. Khan, M.O.F.; Keiser, J.; Amoyay, P.N.A.; Hossain, M.F.; Vargas, M.; Le, J.G.; Simpson, N.C.; Roewe, K.D.; Carder Freeman, T.N.; Hasley, T.R.; et al. Discovery of Antischistosomal Drug Leads Based on Tetraazamacrocyclic Derivatives and Their Metal Complexes. *Antimicrob. Agents Chemother.* **2016**, *60*, 5331–5336. [[CrossRef](#)] [[PubMed](#)]
47. Rohovec, J.; Gyepes, R.; Cisarova, I.; Rudovsky, J.; Lukes, I. Nucleophilic reactivity of perhydro-3,6,9,12-tetraazacyclopenteno[1,3-*fg*]acenaphthylene. A unified approach to *N*-monosubstituted and *N,N'*-disubstituted cyclen derivatives. *Tetrahedron Lett.* **2000**, *41*, 1249–1253. [[CrossRef](#)]
48. Le Baccon, M.; Chuburu, F.; Toupet, L.; Handel, H.; Soibinet, M.; Deschamps-Olivier, I.; Barbier, J.-P.; Aplincourt, M. Bis-aminals: Efficient tools for bis-macrocyclic synthesis. *New J. Chem.* **2001**, *25*, 1168–1174. [[CrossRef](#)]
49. Hubin, T.J.; McCormick, J.M.; Collinson, S.R.; Alcock, N.W.; Busch, D.H. Ultra rigid cross-bridged tetraazamacrocycles as ligands—The challenge and the solution. *Chem. Commun.* **1998**, *16*, 1675–1676. [[CrossRef](#)]
50. Hubin, T.J.; Walker, A.N.; Davilla, D.J.; Carder Freeman, T.N.; Epley, B.M.; Hasley, T.R.; Amoyaw, P.N.A.; Jain, S.; Archibald, S.J.; Prior, T.J.; et al. Tetraazamacrocyclic derivatives and their metal complexes as antileishmanial leads. *Polyhedron* **2019**, *163*, 42–53. [[CrossRef](#)]
51. Groom, C.R.; Bruno, I.J.; Lightfoot, M.P.; Ward, S.C. The Cambridge Structural Database. *Acta Cryst.* **2016**, *B72*, 171–179. [[CrossRef](#)]
52. Hubin, T.J.; McCormick, J.M.; Alcock, N.W.; Clase, H.J.; Busch, D.H. Crystallographic characterization of stepwise changes in ligand conformations as their internal topology changes and two novel cross-bridged tetraazamacrocyclic Copper(II) complexes. *Inorg. Chem.* **1999**, *38*, 4435–4446. [[CrossRef](#)]
53. AlHaddad, N.; Lelong, E.; Suh, J.-M.; Cordier, M.; Lim, M.H.; Royal, G.; Platas-Iglesias, C.; Bernard, H.; Tripier, R. Copper(II) and zinc(II) complexation with *N*-ethylene hydroxycyclams and consequences on the macrocyclic backbone configuration. *Dalton Trans.* **2022**, *51*, 8640–8656. [[CrossRef](#)] [[PubMed](#)]
54. Woodin, K.S.; Heroux, K.J.; Boswell, C.A.; Wong, E.H.; Weisman, G.R.; Niu, W.; Tomellini, S.A.; Anderson, C.J.; Zakharov, L.N.; Rheingold, A.L. Kinetic inertness and electrochemical behavior of Cu(II) tetraazamacrocyclic complexes: Possible implications for in vivo stability. *Eur. J. Inorg. Chem.* **2005**, *7*, 4829–4833. [[CrossRef](#)]
55. Hubin, T.J.; Alcock, N.W.; Morton, M.D.; Busch, D.H. Synthesis, structure, and stability in acid of copper(II) and zinc(II) complexes of cross-bridged tetraazamacrocycles. *Inorg. Chim. Acta* **2003**, *348*, 33–40. [[CrossRef](#)]
56. Walker, A.N.; Ayala, M.A.; Mondal, S.; Bergagnini, M.C.; Bui, P.J.D.; Chidester, S.N.; Doeden, C.I.; Esjornson, L.; Sweany, B.R.; Garcia, L.; et al. A Bridge Too Far? Comparison of Transition Metal Complexes of Dibenzyltetraazamacrocycles with and without Ethylene Cross-Bridges: X-ray Crystal Structures, Kinetic Stability, and Electronic Properties. *Molecules* **2023**, *28*, 895. [[CrossRef](#)]
57. Busch, D.H. The Compleat Coordination Chemistry—One Practitioner's Perspective. *Chem. Rev.* **1993**, *93*, 847–860. [[CrossRef](#)]

58. Schubert, U.S.; Andres, P.R. New functional polymers and materials based on 2,2':6'2''-terpyridine metal complexes. *Adv. Mater.* **2004**, *16*, 1043–1068.
59. Park, J.; Pasupathy, A.N.; Goldsmith, J.I.; Chang, C.; Yaish, Y.; Petta, J.R.; Rinkoski, M.; Sethna, J.P.; Abruna, H.D.; McEuen, P.L.; et al. Coulomb blockade and the Kondo effect in single-atom transistors. *Nature* **2002**, *417*, 722–725. [[CrossRef](#)]
60. Ledwon, P.; Ovsianikova, D.; Jarosz, T.; Gogoc, S.; Nitschke, P.; Domagala, W. Insight into the properties and redox states of n-dopable conjugated polymers based on naphthalene diimide units. *Electrochim. Acta* **2019**, *307*, 525–535. [[CrossRef](#)]
61. Kulthanan, K.; Nuchkull, P.; Varothai, S. The pH of water from various sources: An overview for recommendation for patients with atopic dermatitis. *Asia Pacific. Allergy* **2013**, *3*, 155–160. [[CrossRef](#)]
62. Bayabil, H.K.; Teshome, T.; Li, Y.C. Emerging Contaminants in Soil and Water. *Front. Environ. Sci.* **2022**, *10*, 873499. [[CrossRef](#)]
63. Wang, J.; Chu, L.; Wojnárovits, L.; Takács, E. Occurrence and fate of antibiotics, antibiotic resistant genes (ARGs) and antibiotic resistant bacteria (ARB) in municipal wastewater treatment plant: An overview. *Sci. Total Environ.* **2020**, *744*, 140997. [[CrossRef](#)] [[PubMed](#)]
64. Niang, M.; Reichard, J.F.; Maier, A.; Talaska, G.; Ying, J.; Domingo, J.S.; Varughese, E.; Boczek, L.; Huff, E.; Reponen, T. Ciprofloxacin- and azithromycin-resistant bacteria in a wastewater treatment plant. *J. Occup. Environ. Hyg.* **2023**, *20*, 219–225. [[CrossRef](#)] [[PubMed](#)]
65. Mangalgi, K.P.; Blaney, L. Elucidating the Stimulatory and Inhibitory Effects of Dissolved Organic Matter from Poultry Litter on Photodegradation of Antibiotics. *Environ. Sci. Technol.* **2017**, *51*, 12310–12320. [[CrossRef](#)] [[PubMed](#)]
66. Mangalgi, K.P.; Timko, S.A.; Gonsior, M.; Blaney, L. PARAFAC Modeling of Irradiation- and Oxidation-Induced Changes in Fluorescent Dissolved Organic Matter Extracted from Poultry Litter. *Environ. Sci. Technol.* **2017**, *51*, 8036–8047. [[CrossRef](#)]
67. Mangalgi, K.P.; Patton, S.; Wu, L.; Xu, S.; Ishida, K.P.; Liu, H. Optimizing Potable Water Reuse Systems: Chloramines or Hydrogen Peroxide for UV-Based Advanced Oxidation Process? *Environ. Sci. Technol.* **2019**, *53*, 13323–13331. [[CrossRef](#)]
68. Xu, A.; Xiong, H.; Yin, G. Decolorization of Dye Pollutants by Manganese Complexes with Rigid Cross-Bridged Cyclam Ligands and Its Mechanistic Investigations. *J. Phys. Chem. A* **2009**, *113*, 12243–12248. [[CrossRef](#)]
69. Dolomanov, O.V.; Bourhis, L.J.; Gildea, R.J.; Howard, J.A.K.; Puschmann, H.X. OLEX2: A Complete Structure Solution, Refinement and Analysis Program. *J. Appl. Cryst.* **2009**, *42*, 339–341. [[CrossRef](#)]
70. Sheldrick, G.M. SHELXT-Integrated Space-Group and Crystal-Structure Determination. *Acta Cryst.* **2015**, *A71*, 3–8. [[CrossRef](#)]
71. Sheldrick, G.M. Crystal Structure Refinement with SHELXL. *Acta Cryst.* **2015**, *C71*, 3–8. [[CrossRef](#)]

Disclaimer/Publisher's Note: The statements, opinions and data contained in all publications are solely those of the individual author(s) and contributor(s) and not of MDPI and/or the editor(s). MDPI and/or the editor(s) disclaim responsibility for any injury to people or property resulting from any ideas, methods, instructions or products referred to in the content.